

# Gas migration pathways, controlling mechanisms and changes in sediment acoustic properties observed in a controlled sub-seabed CO<sub>2</sub> release experiment



Melis Cevatoglu<sup>a,\*</sup>, Jonathan M. Bull<sup>a</sup>, Mark E. Vardy<sup>a</sup>, Thomas M. Gernon<sup>a</sup>,  
Ian C. Wright<sup>b</sup>, David Long<sup>c</sup>

<sup>a</sup> University of Southampton, National Oceanography Centre Southampton, Waterfront Campus, European Way, Southampton SO14 3ZH, UK

<sup>b</sup> National Oceanography Centre, University of Southampton Waterfront Campus, European Way, Southampton SO14 3ZH, UK

<sup>c</sup> British Geological Survey, Murchison House, West Mains Road, Edinburgh EH9 3LA, UK

## ARTICLE INFO

### Article history:

Received 28 April 2014

Received in revised form 28 February 2015

Accepted 10 March 2015

Available online 4 April 2015

### Keywords:

CO<sub>2</sub> injection

2D seismic reflection

Gas migration

Reflection coefficient

Attenuation

## ABSTRACT

Carbon capture and storage (CCS) is a key technology to potentially mitigate global warming by reducing carbon dioxide (CO<sub>2</sub>) emissions from industrial facilities and power generation that escape into the atmosphere. To broaden the usage of geological storage as a viable climate mitigation option, it is vital to understand CO<sub>2</sub> behaviour after its injection within a storage reservoir, including its potential migration through overlying sediments, as well as biogeochemical and ecological impacts in the event of leakage.

The impacts of a CO<sub>2</sub> release were investigated by a controlled release experiment that injected CO<sub>2</sub> at a known flux into shallow, under-consolidated marine sediments for 37 days. Repeated high-resolution 2D seismic reflection surveying, both pre-release and syn-release, allows the detection of CO<sub>2</sub>-related anomalies, including: seismic chimneys; enhanced reflectors within the subsurface; and bubbles within the water column. In addition, reflection coefficient and seismic attenuation values calculated for each repeat survey, allow the impact of CO<sub>2</sub> flux on sediment acoustic properties to be comparatively monitored throughout the gas release. CO<sub>2</sub> migration is interpreted as being predominantly controlled by sediment stratigraphy in the early stages of the experiment. However, either the increasing flow rate, or the total injected volume become the dominant factors determining CO<sub>2</sub> migration later in the experiment.

© 2015 The Authors. Published by Elsevier Ltd. This is an open access article under the CC BY license (<http://creativecommons.org/licenses/by/4.0/>).

## 1. Introduction

Carbon capture and storage (CCS) is considered a promising technology to mitigate anthropogenically driven climate change which would enable the continued use of fossil fuels, while contributing on the order of 15–50% of the total climate change mitigation effort until 2100 (Katzner et al., 2007). CCS involves capturing CO<sub>2</sub> from industrial facilities and energy-related sources, transporting it to a storage location, and sequestering it over geologic timescales, with the aim of avoiding its release into the atmosphere. Geological storage is considered the most viable given the overall available storage capacity (at least 2000 gigatonnes (Gt) of CO<sub>2</sub>), and the maturity of current technologies within use by the

oil industry (Metz et al., 2005; Celia and Nordbotten, 2009; Pires et al., 2011).

Associated with the growing interest in CCS as an effective climate mitigation technology, there is an emerging public debate concerning the associated operational and in situ risks of leakage. Various factors leading to leakage can be identified within the surface and subsurface. Failure of injection facilities, including pipelines and wellheads on the surface, as well as injection wells within the subsurface are operational risks. Inadequately completed abandoned wells, insufficient/incomplete top seals or existing faults can cause the ascent of resident fluids (Lackner and Brennan, 2009; Upham and Roberts, 2011). The increase in the subsurface pressure may lead to undesirable geomechanical and hydrodynamical effects, potentially opening pre-existing fractures and/or initiating new fracturing, as well as, triggering seismicity in some cases (Bachu, 2008). Such CO<sub>2</sub> leakage could have significant damaging effects to the local environment, with elevated CO<sub>2</sub> levels known to be toxic to ecosystems, as well as contamination

\* Corresponding author. Tel.: +44 2380 59 6666.

E-mail address: [M.Cevatoglu@soton.ac.uk](mailto:M.Cevatoglu@soton.ac.uk) (M. Cevatoglu).

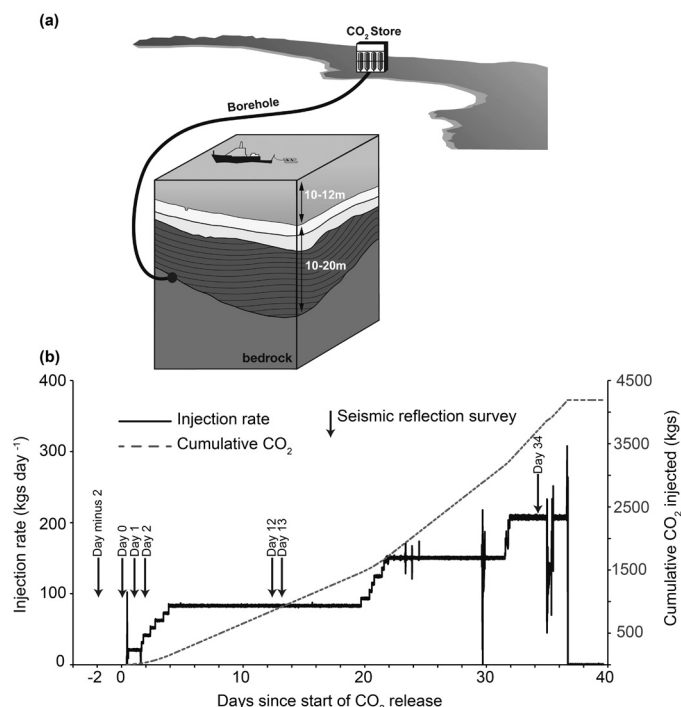


**Fig. 1.** Schematic overview of CO<sub>2</sub> release experiment, changes in total gas injection flux and timing of 2D seismic reflection surveys. (a) A stainless steel lined borehole was connected to a controlled CO<sub>2</sub> supply located onshore, with a 5 m long diffuser located 12 m below the sea floor. The diffuser (black dot) was located at the interface between bedrock and layered glacio-marine sedimentary sequence, which is overlain by an unlayered sequence. Observations were conducted using in-situ, boat towed and diver deployed instrumentation; this paper focusses on the analysis of repeated 2D seismic reflection surveys. (b) Gas injection flux during the experiment and the dates at which 2D seismic reflection surveys were completed pre-release and during the CO<sub>2</sub> release (black arrows; see also Table 1).

of surface waters, decrease in pH and resulting ocean acidification, all being possible outcomes in the medium to long term (Benson et al., 2002; Damen et al., 2006). CO<sub>2</sub> leakage causes an additional carbon input into the atmosphere, and therefore represents a loss of value, or even calling into question CCS operations. Impurities, including H<sub>2</sub>S and SO<sub>2</sub>, that may be present in leaking CO<sub>2</sub>, also have significant environmental impacts (West et al., 2005).

Large-scale implementation of CCS as a viable climate mitigation option requires a much improved understanding of the fate of the injected CO<sub>2</sub> in the subsurface, including its migration and subsequent potential impacts on the marine environment. The goal of the controlled CO<sub>2</sub> release experiment, Quantifying and monitoring potential ecosystem impacts of geological carbon storage (QICS), conducted in Ardmucknish Bay Oban, Scotland (Fig. 1a), was to simulate leakage into the near-surface from geological storage sites, and thus improve our understanding of the behaviour of the injected CO<sub>2</sub> in the subsurface, critical injection rates leading to leakage, amount of leakage, and resulting physical, geochemical, and environmental impacts (Blackford et al., 2014). This paper focuses specifically on the analysis of high-resolution

near-surface 2D chirp and boomer seismic reflection data, together with multibeam bathymetry imagery, acquired before, and during CO<sub>2</sub> release. These data allow an understanding of the CO<sub>2</sub> migration within the subsurface and into the overlying water column, as well as impacts of CO<sub>2</sub> injection on sediment acoustic properties, namely reflectivity and seismic attenuation.

## 2. The QICS experiment

As part of the QICS experiment, a narrow borehole terminating in under-consolidated, shallow marine sediments was drilled from land in Ardmucknish Bay Oban, during February 2012 (Fig. 1a). At the end of the borehole, a 5 m long well screen was installed at a depth of 12 m below the seabed to operate as a diffuser, allowing controlled CO<sub>2</sub> release into sediments from the 17th of May 2012 until the 23rd of June 2012 (Table 1). Details of the drilling operation, and controls on the subsea location of the pipeline are given in Taylor et al. (2015). CO<sub>2</sub> injection rate was increased up to 210 kgs day<sup>-1</sup> from the beginning of the QICS experiment (17/05/2012, Day 0) until Day 37 (23/06/2012) (Fig. 1b). The total amount of CO<sub>2</sub> injected during the 37-day release was c. 4200 kgs (Taylor et al., 2015).

Numerous monitoring strategies were deployed to track the injected CO<sub>2</sub>, detect leakage from the subsurface into the overlying water column, and potentially ultimately into the atmosphere. The period after the cessation of CO<sub>2</sub> injection was also investigated to see if and how the system stabilised post-release, and how these related/differed from the initial conditions. A comprehensive dataset, consisting of multibeam bathymetry, 2D seismic reflection, passive hydroacoustics (Berges et al., 2015), geochemistry, microbiology, macroecology, camera and video surveys, were acquired covering pre-release, syn-release, and the recovery period stages (up to 90 days after cessation of injection), to evaluate the interaction of injected CO<sub>2</sub> with the marine environment. In this paper, we report the results of repeated 2D seismic reflection profiling that was used to determine the spatial and temporal propagation mechanisms of the gaseous CO<sub>2</sub> and assess its role in changing sediment acoustic properties.

### 2.1. Subsurface structure of the QICS site

The QICS site was selected as being suitable for the controlled CO<sub>2</sub> release for several reasons, including: proximity to an onshore drill site; having bedrock that was conducive to drilling; and having a suitable sequence and thickness of sediments above bedrock offshore for the drill pipe to terminate within. High-resolution 2D seismic imaging and sediment coring show that the site comprises up to 20 m of sediment overlying glacial till/bedrock, under 10–12 m depth of water within 350 m range of a drill site on the northern shoreline of Ardmucknish Bay (Taylor et al., 2015). The pre-release boomer data suggest that it is possible to distinguish between the glacial till and bedrock without drilling so that an undisturbed location with minimal till coverage was selected for the gas delivery borehole (Taylor et al., 2015). Multi-beam bathymetry data collected before the experiment showed a

**Table 1**

Description of the 2D seismic reflection datasets collected during the QICS experiment in Ardmucknish Bay and associated CO<sub>2</sub> injection rates.

Days	Description	Seismic source	CO <sub>2</sub> injection rate (kgs day <sup>-1</sup> )
15/05/2012	Pre-release (Day minus 2)	Chirp	none
17/05/2012	1st day of release (Day 0)	Chirp	20
18/05/2012	2nd day of release (Day 1)	Chirp	20
19/05/2012	3rd day of release (Day 2)	Chirp	45
29/05/2012	12 days after release (Day 12)	Chirp	85
30/05/2012	13 days after release (Day 13)	Chirp	85
20/06/2012	34 days after release (Day 34)	Boomer	210

featureless seabed with water depths ranging from 5 m to 30 m with no evidence of pockmarks.

Analysis of sediment cores (including Core 6) collected 200 m south of the CO<sub>2</sub> injection site (Fig. 2 and Fig. 3a), shows that the surficial sediments comprised a c. 1.5 m thick layer of coarse to very coarse sand and gravel, overlying a c. 2 m thick fine sand layer (see Taylor et al. 2015 for a detailed description of the regional stratigraphy). Underlying the fine sand layer is a laminated mud, with the interface appearing as a sharp decrease in grain size (Fig. 2), c. 3–4 m below the seabed. Regional 2D seismic reflection data suggest that this lower sediment unit is c. 15 m thick in total (Fig. 4). In this study the boundary between the near-surface coarse sand and gravel, and fine sand is defined as Horizon 1, and the boundary between the fine sand and the underlying laminated mud as Horizon 2 (Table 2). Taylor et al. (2015) map Horizon 2 as the top of an extensive, highly layered seismic facies (SSS II) interpreted as being glacio-marine deposition, while the fine sand corresponds to their facies SSS III, which is one of several stacked, erosional, acoustically transparent, fluvial units.

This stratigraphy is in agreement with 2D seismic data collected previously in Loch Etive (Fig. 3a), located 6 km north of Oban, showing two seismic sequences separated by a distinct reflector “E1” with modern fluvial sediments, less than 5 m thick, overlying 10–50 m thick glacio-marine sediments (Howe et al., 2002; Nørgaard-Pedersen et al., 2006). The unconformity “E1” corresponds to the erosional surface Horizon 2 in our study, and represents an abrupt change in the sedimentary regime in Ardmucknish Bay from glacially influenced conditions (Younger Dryas; 12.9–11.7 ka BP) with silty-muddy sediments to overlying coarser-grained sandy-silty fluvial sediments deposited during the Holocene (Fig. 2).

### 3. Materials and methods

#### 3.1. Multibeam bathymetry and 2D seismic reflection data acquisition and processing

Seven high-resolution 2D seismic reflection surveys (176 chirp and 18 boomer profiles, totalling 65 km of data) were acquired in

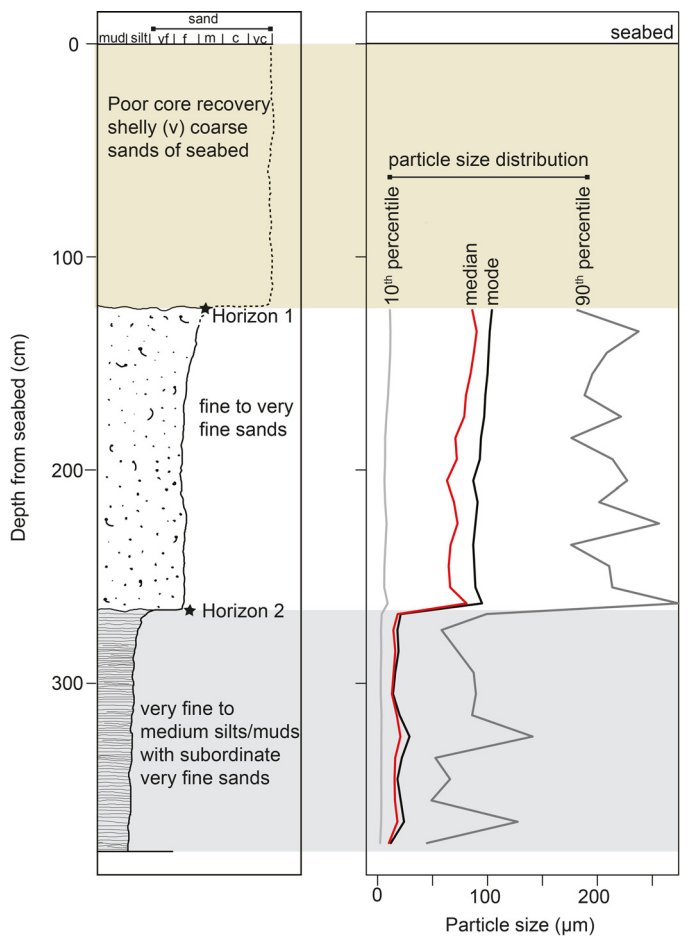


Fig. 2. Detailed stratigraphy and grain-size distribution of sediments within Core 6 (position shown in Fig. 3a). The seabed is composed of coarse-grained shelly sediments which were only partially recovered. The positions of stratigraphic boundaries that are linked to seismic horizons Horizon 1 and Horizon 2 are shown. Previous studies date Horizon 2 to be of early Holocene age (Howe et al., 2002).

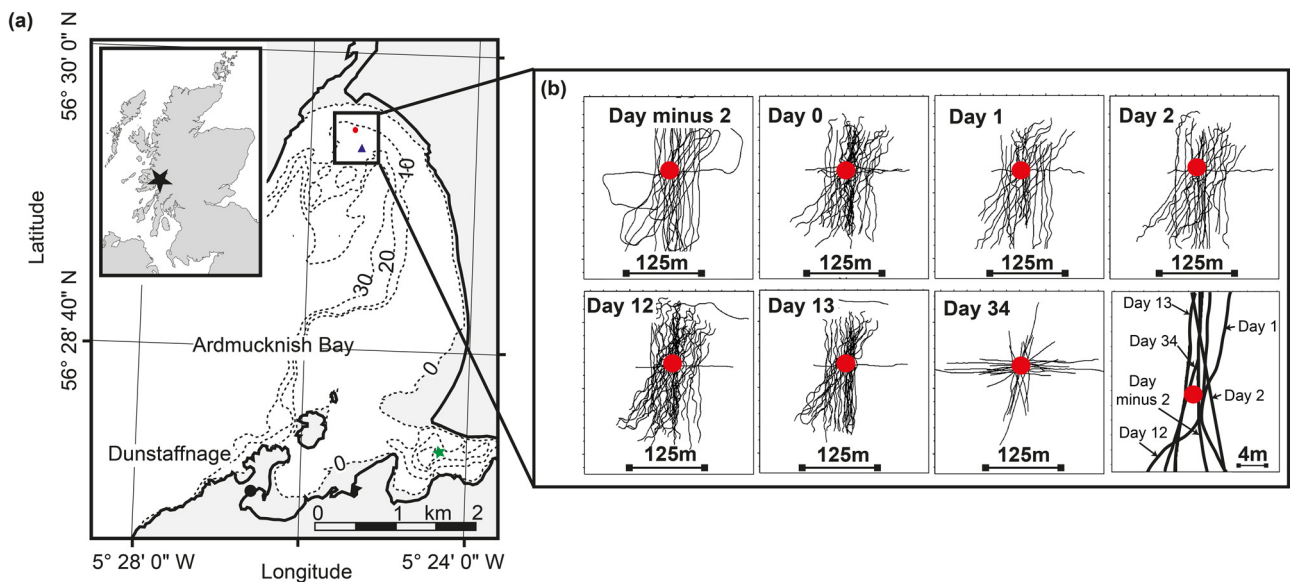
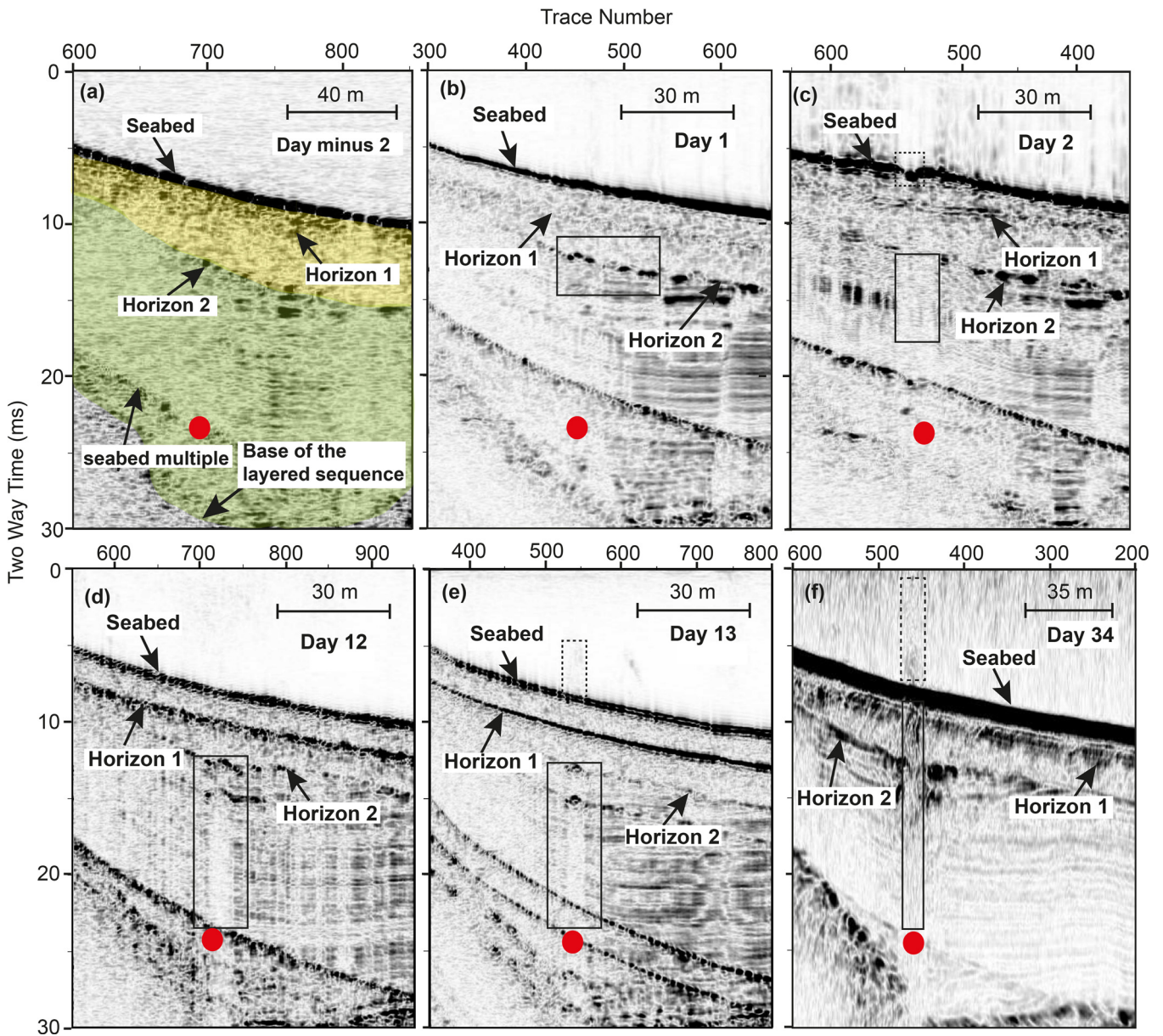


Fig. 3. Detailed location map of the experiment site and 2D seismic reflection profiles within Ardmucknish Bay. (a) Diffuser (dark gray dot) and position of Core 6 (black triangle), superimposed on the bathymetry data (10 m contours). Entrance to Loch Etive is indicated by the black rectangle. (b) Location maps of 2D seismic profiles acquired on different days; chirp data were acquired on Day minus 2 to Day 13; while boomer data were acquired on Day 34. The bottom right box illustrates track lines of the seismic data illustrated in Fig. 4a–f. The diffuser is indicated by the dark gray dot in each case.



**Fig. 4.** Time-lapse 2D seismic reflection data, illustrating CO<sub>2</sub> migration within under-consolidated sediments around the diffuser, Ardmucknish Bay. The position of each seismic profile is given in Fig. 3b. (a) Pre-release chirp data. There is no evidence for gas on the 2D seismic data before CO<sub>2</sub> injection. Sandy–silty fluvial sediments are located above Horizon 2, and silty–muddy glacio-marine sediments are located below Horizon 2. (b) Day 1 chirp data. Following gas release, the reflectivity of Horizon 2 has slightly increased (black rectangle). (c) Day 2 chirp data. CO<sub>2</sub> injection has caused acoustic blanking within sediments (black rectangle), as well as formation of pockmark on the seabed (black dashed rectangle) due to upward migration of CO<sub>2</sub> from the diffuser. There is no clear acoustic evidence of gas between Horizon 2 and the seabed. (d) Day 12 chirp data. Seismic chimneys (black rectangle) below Horizon 2 are interpreted to be caused by the acoustic impedance contrast in the presence of gas. The topmost part of the chimneys shows increase in the reflectivity. No gas was observed between Horizon 2 and the seabed on the 2D seismic data. (e) Day 13 chirp data. Seismic chimneys detected (black rectangle) within the muddy sediments, below Horizon 2. Enhanced reflectors correspond to the topmost part of the chimneys. Bubbles imaged within the water column (black dashed rectangle). (f) Day 34 boomer data. Seismic chimneys (black rectangle) have reached the seabed, without being trapped by Horizon 2. Leakage of CO<sub>2</sub> from the seabed, indicated by the water column acoustic anomalies (dashed black rectangle). The diffuser at 12 m depth below the seabed is indicated by dark gray dot on each figure. The seabed multiple and base of the layered sequence are also indicated by black arrows. Seabed depths vary slightly between the days due to small change in location.

**Table 2**

Seismo-stratigraphic horizons imaged on the 2D seismic reflection data, Ardmucknish Bay. Depths are those observed at the diffuser location. From previous studies, Horizon 2 was dated to early Holocene (Howe et al., 2002), and corresponds to the boundary between modern fluvial sandy sediments above, and to glacio-marine finer-grained sediments below. See main text for more details.

Horizon	Depth	Description
Seabed	0 m	High amplitude and continuous, undulating seismic reflector overlying reflection free unit
Horizon 1	~1.5 m	Sub-parallel to seabed, separating two reflection free units
Horizon 2	~3–4 m	Continuous reflector with significant topography which erosionally truncates the underlying unit. Separates reflection free unit above from underlying unit with regularly spaced sub-parallel reflections
Base of the layered sequence	~15/16 m	Undulating reflector with high seismic amplitude overlying a zone with chaotic reflectivity. Marks base of unit with simple sub-parallel reflectors. Seismic imaging is limited beneath this reflector

Ardmucknish Bay covering both pre-release and CO<sub>2</sub>-release stages (Table 1; Fig. 3a and b). Line spacing ranged from 5 m to 15 m, with closer spacing around the diffuser, while the length of the 2D seismic reflection profiles varied between 250 m and 400 m (Fig. 3a and b). Multibeam bathymetry data were acquired using a Kongsberg EM 2040-07 echosounder, and tidally corrected. Technical details of the 2D seismic reflection and multibeam bathymetry surveys are summarized in Table 3.

Chirp transducers and a boomer plate were both mounted on catamarans towed behind the survey vessel, and all 2D seismic reflection data were corrected for layback (Table 1). Boomer data were band-pass filtered within the frequency range 200–500–4000–6000 Hz. The seismic processing flow applied to the chirp data included correlation with the source sweep (Quinn et al., 1998), Ormsby band-pass filtering, 3-trace mixing, true amplitude recovery correction and instantaneous amplitude correction. There is no migration applied to the 2D seismic data. Where, Chirp data were used for physical property determination, only correlation was applied; no further processing was undertaken. Finally, tidal corrections were applied to the chirp and boomer data using the pre-release tidally-corrected swath bathymetry mosaic.

It is worth noting that the water and target depths investigated in this study, c. 10–12 m and less than 15 m, respectively, are significantly shallower than that typically investigated by the oil and gas industry. The frequency range of the high-resolution 2D seismic systems (1.5–13.0 kHz for chirp and 0.5–4.0 kHz for boomer) results in an improved vertical seismic resolution of tens of cm compared to a few metres for typical industry seismic data. However, the data presented here consist of a repeat set of 2D seismic reflection profiles, which has inherent limitations in terms of tow depth, tidal state, navigation and tow speed repeatability, as well as wavefield sampling (and therefore imaging) when compared to the 3D marine surveying, typical of industry surveys. Readers are advised to bear in mind these differences in seismic source and acquisition methodology when comparing the presented results with previously published seismic time-lapse studies of CCS sites (Arts et al., 2008; Chadwick et al., 2010).

### 3.2. Reflection coefficient and seismic attenuation calculation

Gas within pore spaces will change the bulk acoustic properties of marine sediments. In this paper two attributes of the 2D seismic reflection data, and their spatial and temporal variation, were determined: the reflection coefficient of the seabed and subsurface horizons; and acoustic attenuation of near-surface sediments. These data are then used to infer variations in the spatial distribution and flux of CO<sub>2</sub>.

Following previous work (Anstey, 1977; Warner, 1990; Spence et al., 1995; Bull et al., 1998), the reflection coefficient of the seabed

( $K_{sf}$ ) and a deeper reflector ( $K_{dr}$ ) can be calculated from Eqs. (1) and (2):

$$K_{sf} = \frac{TWT(m)}{TWT(p)} \times \frac{A(m)}{A(p)} \quad (1)$$

$$K_{dr} = K_{sf} \times \frac{TWT(dr)}{TWT(p)} \times \frac{A(dr)}{A(p)} \quad (2)$$

where  $A(p)$ ,  $A(m)$  and  $A(dr)$  represent the seismic amplitudes of the primary seabed reflector, the first multiple of seabed reflector and deeper reflector respectively, while  $TWT(p)$ ,  $TWT(m)$  and  $TWT(dr)$  are the corresponding two-way travel times.

These relationships inherently include a correction for geometrical spreading, which is proportional to the ratio of  $TWT(m)/TWT(p)$  in Eq. (1), and  $TWT(dr)/TWT(p)$  in Eq. (2). Since the application of complex seismic processing algorithms (such as deconvolution) often results in alteration of reflection amplitudes, the 2D seismic data used in the reflection coefficient analysis were simply correlated with the source sweep in chirp data, and band-pass filtered, in the case of boomer data, with no further processing in either. After correlation, a time gate of 1 ms was chosen to analyse amplitude values associated with the seabed and subsurface horizons. It should be noted that the analysis of reflection coefficient is based on the ratio of amplitudes. Therefore, the changes in the raw amplitudes of the whole traces on different survey days due to changes in seismic source and/or survey conditions do not affect our calculations.

The spectral-ratio technique has previously been used to determine the seismic quality factor ( $Q$ ), which is inversely proportional to seismic attenuation ( $\alpha$ ) (Williams et al., 2002; Schock, 2004; Pinson et al., 2008). By combining this technique with a statistically robust regression, it is possible to calculate  $Q$  with an associated confidence interval for the uppermost 30 m of marine sediments (Pinson et al., 2008):

$$\ln \frac{|A_R(f)|}{|A_S(f)|} = \ln \frac{|G_R \times (1 - R_S^2 \times R_R)|}{|R_S|} - \frac{\pi \times f \times \Delta t_R(f)}{Q(f)} \quad (3)$$

where  $A_S(f)$  and  $A_R(f)$  indicate amplitudes of the seabed reflection and horizon of interest beneath the seabed at the frequency  $f$ .  $G_R$ ,  $R_S$  and  $R_R$  correspond to spherical divergence between the seabed and the horizon of interest, reflection coefficient of the seabed, and the horizon of interest, respectively. Finally,  $\Delta t_R(f)$  is the two-way travel time between the seabed and the horizon of interest.

Under the condition of sampling two sub-horizontal reflections,  $G_R$  can be considered to be constant from trace to trace, and also frequency independent. In addition, the target reflection is required to be shallower than the first seabed multiple to avoid delayed energy contaminating the spectra. The effect of noise and local inhomogeneities can be overcome by using multiple traces, which produces a more accurate  $Q$  estimation, but under these conditions we have to assume that  $R_S$  and  $R_R$  are laterally consistent.

**Table 3**  
2D seismic reflection and multibeam bathymetry data acquisition parameters. See Supplementary material for more detail about chirp and boomer seismic survey geometries.

Seismic reflection		Multibeam bathymetry		
Seismic acquisition	Geoacoustics GeoChirp	Applied Acoustics Boomer	Operating frequency	400 kHz
Trace spacing	0.3 m	0.35 m	Pulse length	50 $\mu$ s
Seismic acquisition	4 transducers array, 1.5–13 kHz, 32 ms, sine squared 8th sweep (Gutowski et al., 2002)	Boomer plate operating at 200 J	Swath width	280° (400 beams x 0.7°)
Hydrophone	1 m long, single channel, towed behind the survey vessel	10 m long, single channel, towed behind the survey vessel	Theoretical resolution	4 cm
Pulse rate	0.25 Hz	3 Hz		
Trace length	200 ms	250 ms		
Surveyed area	600 m x 400 m	400 m x 500 m		
Line orientation	NS, EW, NE–SW	EW, NE–SW, NW–SE		
Survey vessel	R/V Seol Mara	R/V White Ribbon		

After selecting suitable traces that clearly image the seabed and the seismic horizon of interest, 2D seismic data were subjected to a sequence of 1 kHz wide zero-phase Ormsby band-pass filters, where the central frequency incremented by 0.25 kHz steps, and reflection amplitudes were extracted for each frequency window. After the application of the spectral-ratio technique to the selected traces, two plots were generated. The spectral signature plot (SSP), which shows the variation of  $\ln(|A_R|/|A_S|)$  and  $\ln(\text{Noise}/|A_S|)$  with frequency, which was used to identify the uncontaminated frequency band containing the attenuation trend, in a way that the selected band contains signal above the background noise, and has a good match between the mean and median values. The average  $Q$  of a sediment package was then calculated by plotting the attenuation trend plot (ATP), showing the variation of  $-\ln(|A_R(f)|/|A_S(f)|)$  with  $\pi f \Delta t_R(f)$  in (3). By means of using simple least-square regression,  $Q$  values are first estimated with 95% confidence interval, and then by fitting the best iteratively reweighted robust least-squares regression curve to the current data points, a robust  $Q$  value is calculated. The analysed 2D seismic data had only minimal processing applied (correlation with source sweep), as further processing would modify the spectral content of the data, and therefore invalidate the  $Q$  calculation. Similarly to reflection coefficient calculation,  $Q$  estimates are based on the ratio of the relevant horizon amplitudes, thus excluding the absolute changes in the raw amplitudes on different survey days.

## 4. Results and analysis

### 4.1. Subsurface seismic stratigraphy

Four horizons were identified around the CO<sub>2</sub> injection area in Ardmucknish Bay from chirp and boomer 2D seismic reflection profiles (see also Section 2.1). The topmost horizon is the seabed, which is a high amplitude slightly undulating reflector, with depth increasing up to c. 15 m with distance from the shore (Figs. 2 and 4). The second horizon, referred to as Horizon 1, is sub-parallel to the seabed, c. 2 ms (around 1.5 m) below it (Figs. 2 and 4). The next horizon, Horizon 2, c. 3–4 m below the seabed, defines the

base of an acoustically transparent, reflection-free deposit, and represents the boundary between this unit and the underlying stratified sedimentary sequence (Figs. 2 and 4). Horizon 2 is a characteristic unconformity, easily traced throughout the 2D seismic dataset, has significant topography, deepening significantly to the W-SW, and erosionally truncates the underlying sequence. The layered sequence beneath Horizon 2 is a thick (up to 40 m) stratigraphic facies, containing regularly spaced sub-parallel reflections (Figs. 2 and 4). The deepest horizon detected on the 2D seismic data corresponds to the base of the layered sedimentary infill (Fig. 4). The base of the layered sedimentary infill is a chaotic seismic horizon with high amplitude seismic reflections and has a highly undulating surface, deepening significantly in the SE while truncating Horizon 2 in the W-SW. The properties of these four key seismic horizons are summarised in Table 2.

Recent work on the depositional history of the Scottish west coast fjords since the last glaciation has revealed the presence of diamict (McIntyre and Howe, 2010), which likely corresponds to the stratigraphic unit below the base of the layered sedimentary infill in this 2D seismic dataset. Thus, we interpret the base of the layered sedimentary infill as being the top of a thin glacial till unit overlying bedrock.

### 4.2. Temporal and spatial evolution of CO<sub>2</sub>-related acoustic anomalies

The 2D seismic reflection data were also interpreted for evidence of gas in the water column and sediment, including: acoustic turbidity; gas blanking; bright spots; reflector terminations; and polarity reversals. The aim of the interpretation was to understand the temporal development of CO<sub>2</sub> migration pathways in the subsurface and overlying water column. Acquisition of pre-release 2D seismic reflection data was crucial for determining the baseline subsurface reflectivity, allowing comparison with 2D seismic data acquired during CO<sub>2</sub> injection. As a result, many CO<sub>2</sub>-related temporal reflectivity changes were observed on the chirp and boomer 2D seismic profiles (Fig. 4a–f).

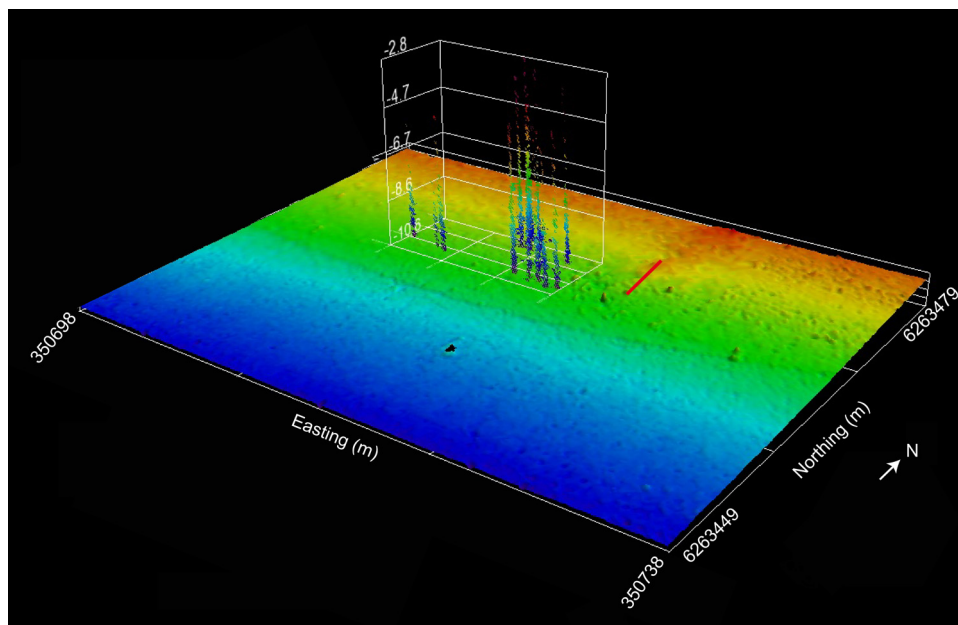


**Fig. 5.** Pockmarks and water column bubbles imaged on the multibeam bathymetry data at Day 34. The location of the gas streams and pockmarks are within the area of chimneys detected on the boomer data. Pockmarks are visible as circular depressions on the seabed south and west of the end of the diffuser (position at depth shown by red line). Many of the pockmarks have gas streams emerging from them, with the height of the bubble streams varying, perhaps reflecting the relative flux emerging from each pockmark.

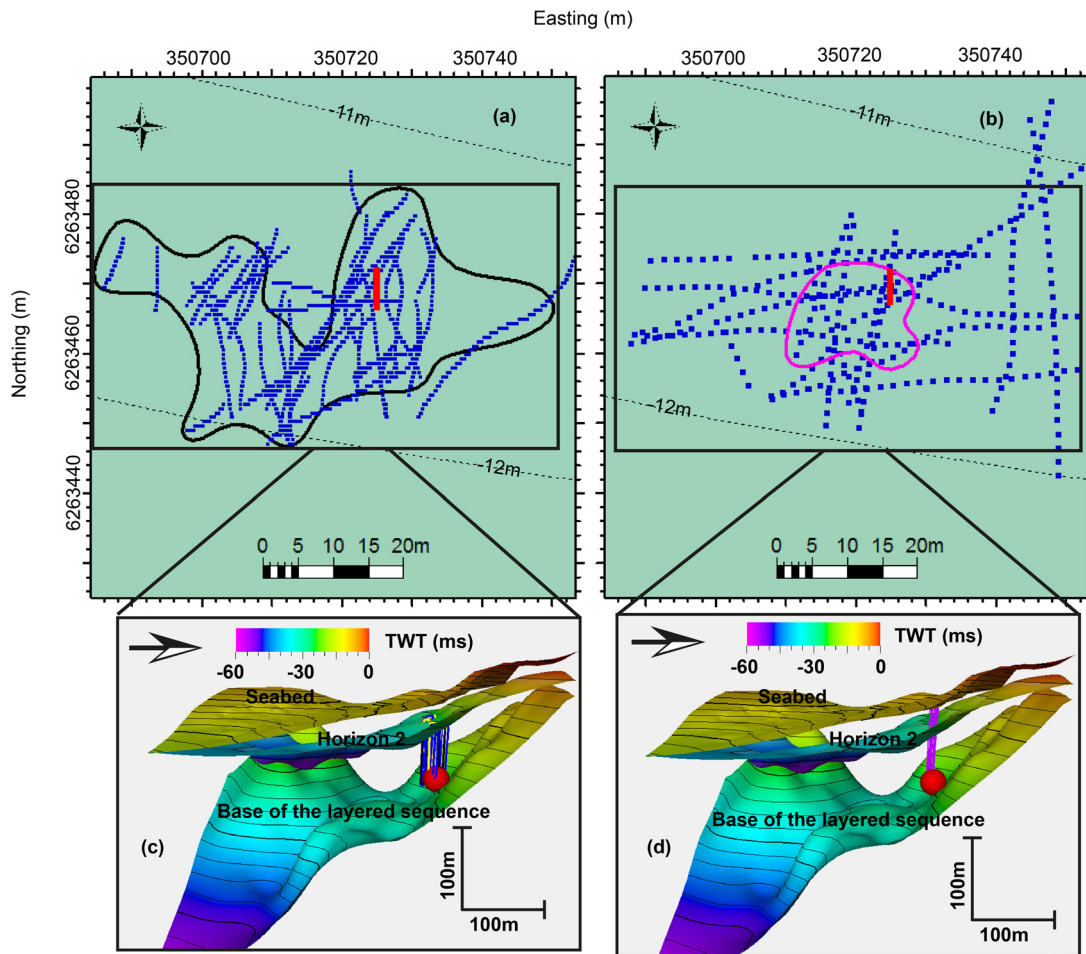


**Fig. 6.** Spatial distribution of CO<sub>2</sub>-related high reflectivity anomalies for Horizon 2 and seismic chimneys within the overburden. (a) Spatial extent of high reflectivity anomalies (blue dots) and seismic chimneys (black polygon) detected on the chirp dataset, from Day 0 to Day 13. Most of the high amplitude anomalies are c. 30 m west of the diffuser (red line). (b) Spatial extent of high reflectivity anomalies (blue dots) and seismic chimneys (pink polygon) detected on the boomer dataset, Day 34. There is an increase in the overall extent of high amplitude anomalies, c. 30 m each side of the diffuser (red line). However, note the significant decrease in the area affected by chimneys at Day 34. (c) 3D image of the key seismic horizons (Seabed, Horizon 2, and Base of the layered sequence) and chirp chimneys (Day 2 chimneys (black polygons), Day 12 chimneys (blue polygons) and Day 13 chimneys (yellow polygons)). From Day 0 to Day 13, seismic chimneys reach Horizon 2. (d) 3D image of the key seismic horizons (Seabed, Horizon 2, and Base of the layered sequence) and boomer chimneys (purple polygons). At Day 34, seismic chimneys are no longer restricted by Horizon 2: they reach the seabed and CO<sub>2</sub> is released into the water column.

Analysis of the pre-release 2D seismic data (Day minus 2) reveals no direct indicators of gas within the subsurface around the CO<sub>2</sub> injection site (Fig. 4a). Over the first two days of release, Day 0 and Day 1, where the CO<sub>2</sub> injection rate/total injected volume was relatively small (Table 1), there is an increase in the reflectivity of Horizon 2, compared to pre-release data (Fig. 4b). With the increase of CO<sub>2</sub> injection rate/total injected volume (Table 1), 2D seismic data show localised, well-defined, low amplitude, vertical transparent zones up to 8 m in width, rising from the diffuser up to Horizon 2, as well as the formation of small scale pockmarks (4.5 m wide, 60 cm deep) on the seabed (Fig. 4c).

With an increased amount of CO<sub>2</sub> injected into the subsurface, by Day 12 and Day 13, Horizon 2 displays enhanced reflectivity and up-warped geometry, but the vertical transparent zones and associated reflector terminations remain confined within the layered sequence below Horizon 2 (Fig. 4d and e). However, water column anomalies are also widely observed on the 2D seismic data (Fig. 4e).

Boomer data collected later in the release period, Day 34, reveal many CO<sub>2</sub> related features, including: enhanced reflectivity for Horizon 2; columnar zones of low and chaotic seismic reflectivity; and water column anomalies (Fig. 4f). Most importantly, following the significant increase in the CO<sub>2</sub> injection rate/total injected volume at Day 34 (Table 1), these vertical acoustic disturbance

columns, which were previously confined within the layered sedimentary sequence below Horizon 2, now reach the seabed, leading to CO<sub>2</sub> leakage directly into water column (Fig. 4f).

Multibeam bathymetry data collected on Day 34 clearly image both pockmarks on the seabed and the column of gas within the water column (Fig. 5) (Blackford et al., 2014). The position of the pockmarks and water column bubbles are all observed up to c. 15 m west of the diffuser (Fig. 5). The height of the gas streams above the seabed varies over the area: bubbles in the immediate vicinity of the diffuser were imaged to rise up to c. 8 m above the seabed, whereas more distal bubbles are observed to rise up to c. 2 m above the seabed (Fig. 5).

Enhanced seismic reflectivity has been shown in various geological settings to be associated with the typical seismic response of sediments containing shallow gas (Petersen et al., 2010; Rajan et al., 2012; Zhang et al., 2012; Yoo et al., 2013). These high seismic amplitudes are caused by the large acoustic impedance contrast between gas-charged and gas-free sediments. Vertical transparent acoustic disturbance zones (Days 2–13), or chaotic and relatively low amplitude internal reflections (Day 34), detected on the 2D seismic data, will henceforth be referred to as seismic chimneys. Seismic chimneys are the acoustic evidence of focused fluid flow pathways, and found commonly associated with upward

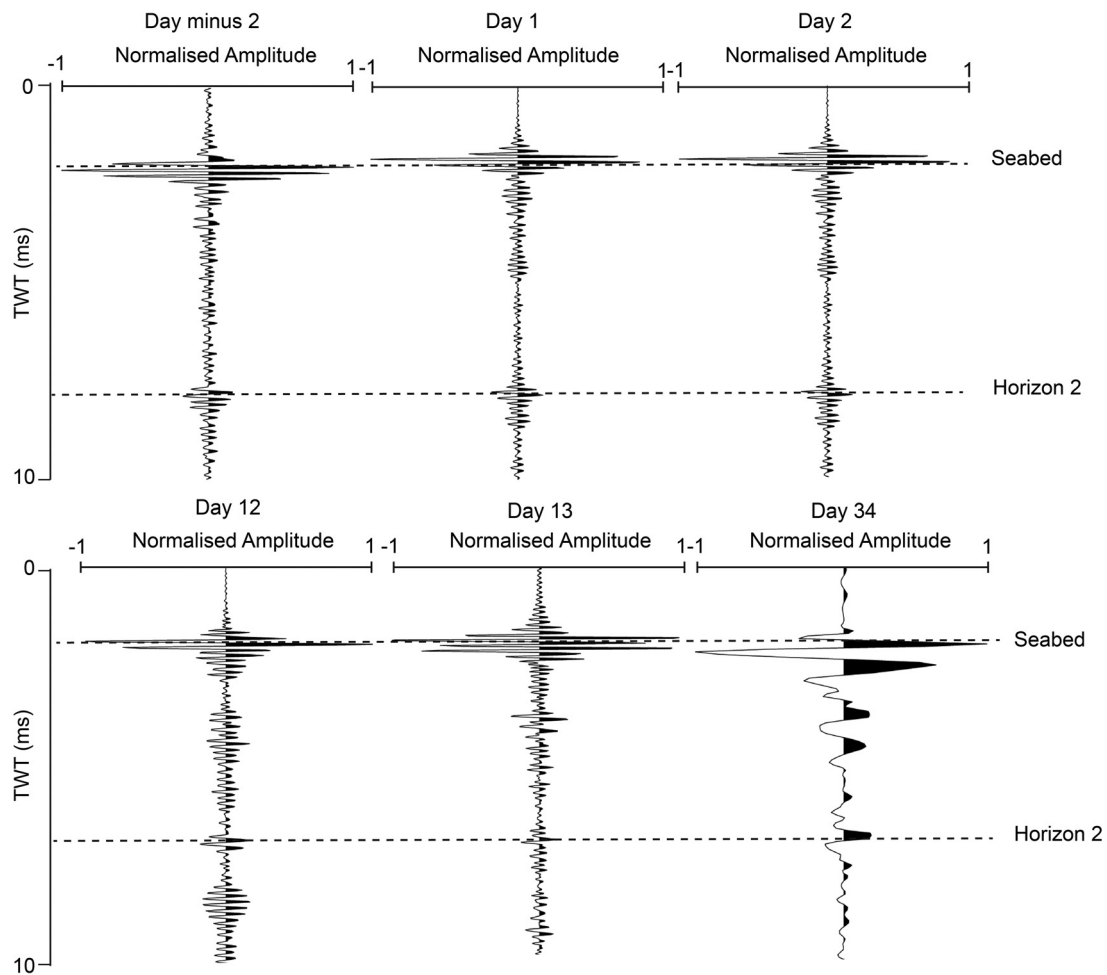


**Fig. 7.** Seismic wiggle traces from outside the chimney area for all days of 2D seismic surveying in Ardmucknish Bay. The seismic traces are normalized by their seabed multiple and 7-trace mixing is applied. The comparison of different days of seismic data within the non-gassy sediments clearly illustrates the coherency of the seismic response outside the chimney area. Small changes in the horizon amplitudes are probably related to the small variations in the spatial location, errors inherent in the repeatability of 2D seismic surveying. Note that the polarity of Horizon 2 is consistently positive outside the chimney area.

hydrocarbon migration from source rocks to the reservoir, and between reservoirs at different depths (Meldahl et al., 2001; Løseth et al., 2009; Baristean et al., 2012). Enhanced reflectors at the crest of seismic chimneys detected at Day 12 and Day 13 (Fig. 4d and e) have previously been well-documented in seismic reflection data, and represent the acoustic impedance contrast in the presence of free-gas within the overburden (Tomasini et al., 2010; Sun et al., 2012). The slightly up-warped internal reflections found within the topmost part of seismic chimneys at Day 12 and Day 13 are possibly related to the sediment deformation caused by the buoyancy of moving gases in the early stages of chimney formation (Cathles et al., 2010; Plaza-Faverola et al., 2011), as free-gas within the sediment pore space would normally cause down-warping associated with the decrease in the seismic velocity. Due to the imperfect spatial repeatability of the 2D seismic lines (Fig. 4), as well as the lack of imaging of individual reflectors within the seismic chimneys, we do not observe the impacts of velocity push-down within the seismic data.

High reflectivity anomalies for Horizon 2, as well as the spatial extent of the seismic chimneys detected on the chirp and boomer datasets were mapped (Fig. 6a and b). In the early stages of the experiment, most of the high reflectivity anomalies are clustered c. 30 m W of the diffuser (Fig. 6a), whereas, in the latter stages, these anomalies are detected over a wider area c. 30 m either side of the diffuser (Fig. 6b). Contrary to the increase in the spatial extent of high reflectivity anomalies with time, the area covered by seismic

chimneys decreases significantly in the latter stages of the experiment, from  $65 \times 40$  m on Days 12 and 13 to  $20 \times 20$  m on Day 34, suggesting a more localized focussed flow at depth above the diffuser at Day 34 (Fig. 6a and b). Fig. 6c and d represent the subsurface horizons and associated chimneys within the black boxes on Fig. 6a and b. Analysis of the occurrence of seismic chimneys reveals that their number increased proportionally with  $\text{CO}_2$  injection rate/total injected volume, with no chimneys on Day 0 and Day 1, a small number of chimneys detected at Day 2, and a significant increase in the number of chimneys at Day 12 onwards (Fig. 6c and d; Table 1).

The seismic response of different horizons (seabed, Horizon 1 and Horizon 2) outside the chimney area is illustrated in Fig. 7. The seismic traces from different survey days on Fig. 7 are chosen to be approximately at the same location within an area not affected by gas flux. The amplitudes are normalised by their seabed multiple, and 7-trace mixing is applied. Slight changes in the seismic amplitudes of the key horizons on different days are probably related to the small variation of the spatial location of these traces; however, the seismic response remains coherent overall.

The temporal propagation of gas is illustrated by the schematic diagram shown in Fig. 8. In the very early stages of the experiment, at Day 0 and Day 1,  $\text{CO}_2$  migrated within the lower layered mud sequence, and reached Horizon 2, revealed by an increase in acoustic impedance contrast between gas-free and gassy sediments (Fig. 8a). Isolated bubble streams were also detected in the water column at this stage, showing that the injected  $\text{CO}_2$  travelled above

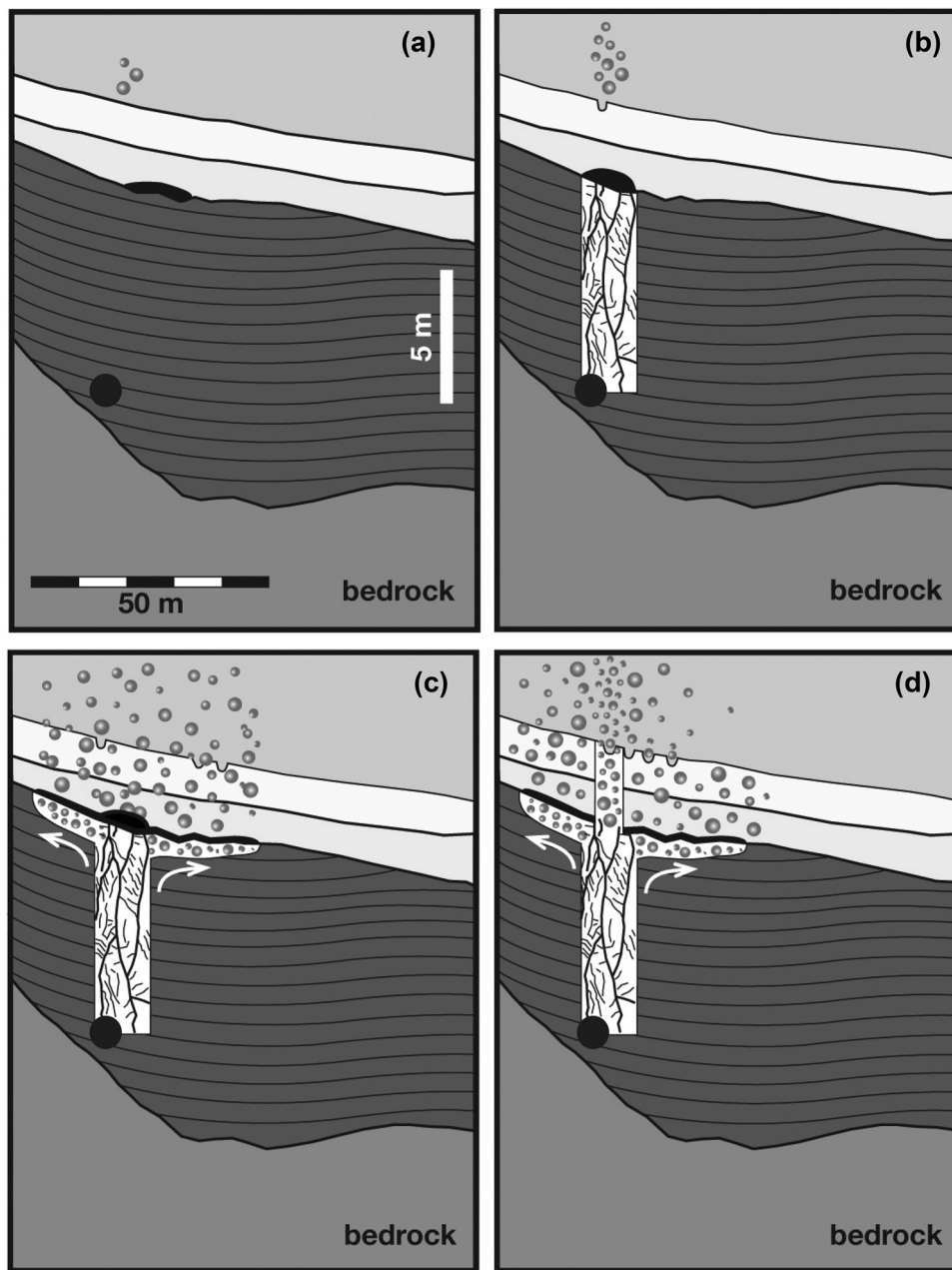


**Fig. 8.** Schematic diagram summarising stages of gas migration revealed by the repeated 2D seismic reflection surveys. (a) Within 24 h gas bubbles were visible in the water column, Horizon 2 has increased reflectivity, but no significant anomalies were detected above Horizon 2. (b) A connected series of fractures allowed propagation of gas through the mud layer which was imaged as chimney structures at Day 2. Formation of pockmarks on the seabed, as well as bubbles detected within the water column. No gas imaged in the overlying sand. (c) With continued gas release, at Day 12 and Day 13, gas spread along the base of the overlying sand layers, as revealed by high reflectivity of Horizon 2. Chimneys below Horizon 2 are frequently imaged, but there is no clear acoustic evidence of gas above Horizon 2. (d) Eventually the overlying sand layer was also fractured and chimney structures are imaged from the diffuser (black dot) up to the seabed at Day 34. Gas bubbles were imaged on 2D seismic reflection profiles in the water column, as well as on the multibeam bathymetry data (Fig. 5). The overall area affected by chimneys is smaller; however, the spatial extent of high reflectivity anomalies for Horizon 2 is larger compared to previous days (Fig. 6a and b).

Horizon 2, despite the lack of clear acoustic evidence within the acoustically transparent sandy unit (Fig. 8a). On Day 2, a few seismic chimneys were formed within the muddy sediments, rising from the diffuser to Horizon 2, allowing the rapid upward transport of CO<sub>2</sub> to Horizon 2 (Fig. 8b). Pockmarks were imaged on the seabed, which were seen by divers to be emitting isolated bubble streams (Fig. 8b). On Day 12 and Day 13, many seismic chimneys were imaged, rising from the diffuser to Horizon 2. Gas had spread along the base of the overlying sand layers, as revealed by the high reflectivity of Horizon 2, and is consistent with this horizon inhibiting/slowing gas migration upward into the overlying sediments (Fig. 8c). More bubbles were observed within the water column

on the 2D seismic reflection data, although no significant acoustic anomalies were detected above Horizon 2 at this stage (Fig. 8c). Eventually, on Day 34, seismic chimneys were imaged from the diffuser to seabed, leading to many more bubbles imaged on the 2D seismic reflection and multibeam bathymetry data, as well as being observed by divers (Fig. 8d).

#### 4.3. Impacts on sediment acoustic properties

##### 4.3.1. Reflection coefficient

Detailed analysis of the 2D seismic reflection data reveals a polarity reversal for Horizon 2 within the chimney area (Fig. 9a),

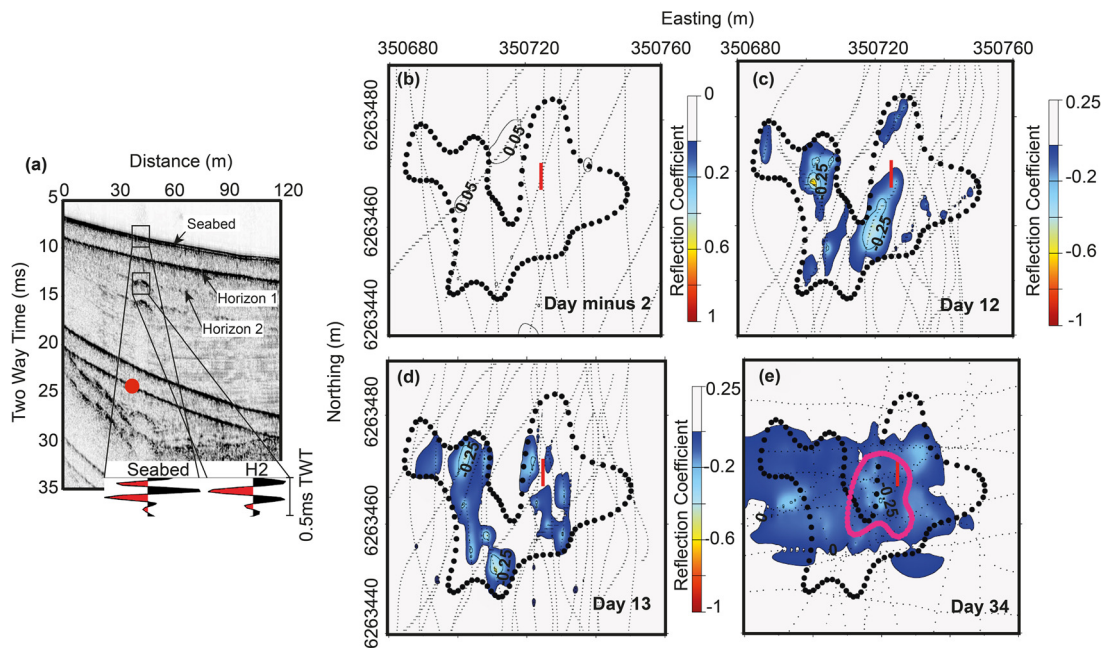


**Fig. 9.** Temporal variation in the reflection coefficient of Horizon 2. (a) 2D seismic profile acquired on Day 12 and inset showing polarity reversal on Horizon 2 due to the presence of CO<sub>2</sub> within the chimney. The seabed has a positive polarity and Horizon 2 has a negative polarity; diffuser indicated by red dot. Horizon 1 is also indicated. (b) The reflection coefficient map prior to CO<sub>2</sub> injection (Day minus 2), showing no significant spatial reflection coefficient anomaly in the area. The outline of the seismic chimney which later developed on Day 12 is indicated by the black dotted polygon. (c) The reflection coefficient map at Day 12. Due to gas injection, significant reflection coefficient reduction for Horizon 2 occurs within the chimney, mostly to the west of the diffuser (red line). (d) The reflection coefficient map at Day 13. There is an obvious decrease in the reflection coefficient within the chimney, to the west of the diffuser. (e) The reflection coefficient map for Horizon 2 at Day 34. Significant reflection coefficient reduction is observed within and outside the seismic chimney area (pink polygon) at Day 34. 2D seismic line locations are shown by the black dashed lines. Mean values of reflection coefficients within and outside the area affected by chimneys are shown in Table 4.

compared to its former signature and that of the seabed (Fig. 7). This is consistent with a reduction in acoustic impedance due to the presence of CO<sub>2</sub> in the pore space. Temporal variation of seismic reflectivity following CO<sub>2</sub> injection was evaluated by determining the reflection coefficients of the seabed and Horizon 2. The pre-release (Day minus 2) seismic reflection dataset allowed a baseline to be determined (Fig. 9b and Fig. 10a). For seismic surveys completed during gas release, the reflection coefficient for the seabed and Horizon 2 were calculated for data affected by prominent CO<sub>2</sub> chimneys, as well as for data without evidence of seismic chimneys (Fig. 9c–e and Fig. 10b–e).

In the pre-release chirp data, there is no significant spatial variation in the reflection coefficient of Horizon 2 in the study area (Fig. 9b); the mean reflection coefficient for Horizon 2 is +0.04 ( $\pm 0.01$ ) (Table 4). However, Horizon 2 reflection coefficient values from Day 12 and Day 13 2D seismic reflection data, show a significant decrease, within the area affected by chimneys, mainly to the west of the diffuser (Fig. 9c and d; Table 4). The mean reflection coefficient is initially +0.11 ( $\pm 0.05$ ) outside the chimney, and reduces to  $-0.12$  ( $\pm 0.1$ ) and  $-0.10$  ( $\pm 0.08$ ) within the chimney area for Days 12 and 13 (Table 4). The east and south of the diffuser area show significant reflectivity variation between Day 12 and Day 13 (Fig. 9c and d). At Day 34, there is a significant reduction in the reflection coefficient of Horizon 2 within the chimney area, as well as an increase in the spatial extent of the area affected by high reflectivity (Fig. 9e). The mean reflection coefficient for Horizon 2 on Day 34 within the chimney is  $-0.11$  ( $\pm 0.04$ ) and +0.05 ( $\pm 0.03$ ) outside the chimney area, with an overall reduction in Horizon 2 reflection coefficient by  $-0.16$  within the chimney at this time (Table 4). At Day 34, the spatial distribution of Horizon 2 reflectivity variations within the chimney area is more uniform (Fig. 9e), compared to the uneven spatial distribution of the reflectivity anomalies observed at Day 12 and Day 13 within the seismic chimney (Fig. 9c and d).

The seabed reflection coefficient map from pre-release chirp data shows that there is no significant spatial variation (Fig. 10a; Table 4). Days 12 and 13 show a general increase in seabed reflectivity compared to the pre-release data (Fig. 10b and c; Table 4). By combining the seabed reflection coefficient values from Days 12 and 13, the difference in the reflection coefficient of the seabed ( $\Delta RC$ ) between Day minus 2 and Days 12–13 (combined anomaly) can be determined (Fig. 10d). The combined anomaly shows the overall area with increased reflectivity for the seabed, and this correlates closely with the position of the subsurface chimneys (Fig. 10d). The seabed reflectivity on Day 34 also shows an increase within the area affected by chimneys, extending to the north of the survey area (Fig. 10e; Table 4). In summary, the temporal changes in seabed reflectivity between Day 12 and Day 34 were found to be within, and in the immediate vicinity of, the area affected by seismic chimneys at depth (Fig. 10b–e).

To better evaluate the variation in the reflectivity of Horizon 2 due to CO<sub>2</sub> injection, the difference in the reflection coefficient of Horizon 2 ( $\Delta RC$ ) between pre-release and syn-release data was also investigated (Fig. 11a–d). From the analysis of the difference in the reflection coefficient of Horizon 2 ( $\Delta RC$ ) between Day minus 2 and Day 12 (Day 12–Day minus 2), a significant decrease in the reflection coefficient of Horizon 2 is observed within the seismic chimney area, mainly to the west of the diffuser (Fig. 11a). Similarly, the reduction in the reflection coefficient of Horizon 2 within the chimney area is remarkable between Day minus 2 and Day 13 (Day 13–Day minus 2) (Fig. 11b). By combining the reflection coefficient values calculated for Horizon 2 from Day 12 and Day 13 within and outside the chimney area (combined anomaly), the overall area with decreased reflection coefficient of Horizon 2 can be identified (Fig. 11c). Finally, the difference in the reflection coefficient of Horizon 2 ( $\Delta RC$ ) between the pre-release data and combined anomaly is calculated (Fig. 11d). All of these maps (Fig. 11a–d) clearly show isolated patches of reflectivity anomalies with significant reductions

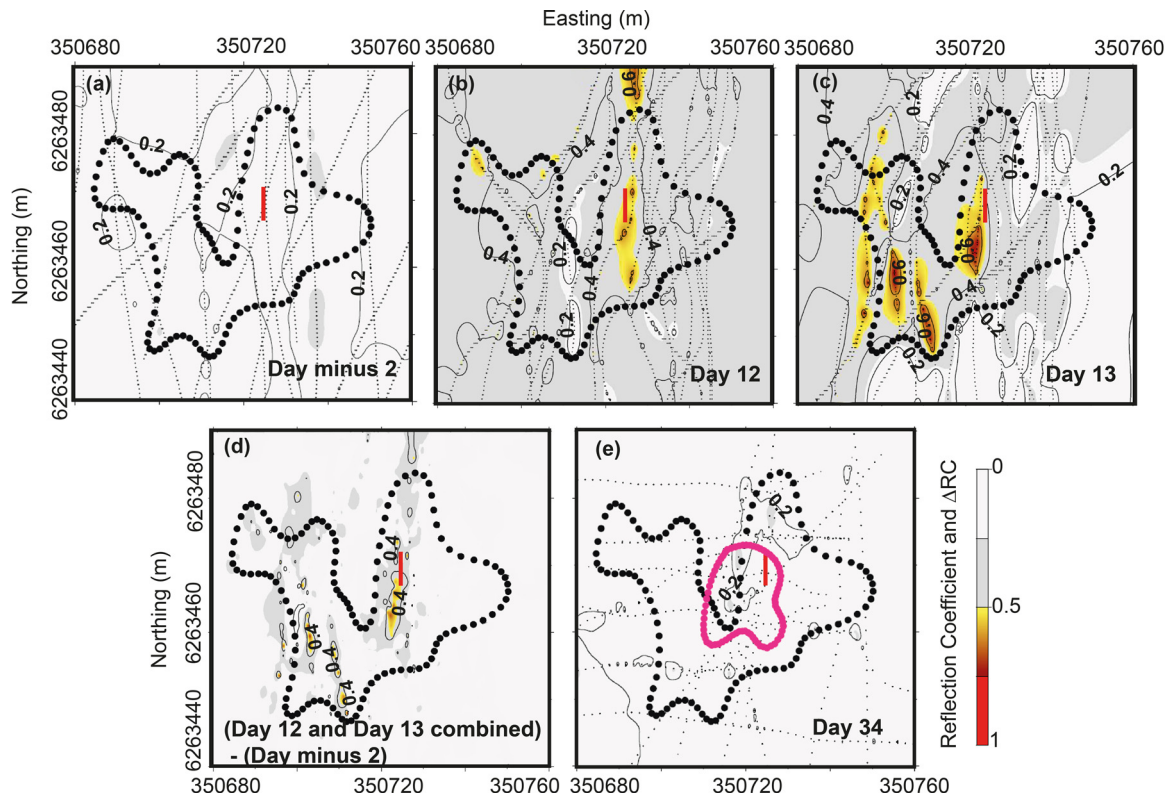


**Fig. 10.** Temporal variation in reflection coefficient of the seabed. (a) The reflection coefficient map prior to CO<sub>2</sub> injection (Day minus 2). There is no significant variation in the seabed reflectivity. The chimney which later developed on Day 12 is indicated by the black polygon. (b) The reflection coefficient map for Day 12. The seabed reflectivity is uniform on either side of the chimney, with the exception of small areas of increased reflectivity at the close proximity of the diffuser (red line), as well as to the west. (c) The reflection coefficient map at Day 13. Large variation in the seabed reflectivity is observed within the chimney area, as well as outside the chimney. (d) The difference in the seabed reflection coefficient ( $\Delta RC$ ), using pre-release and during injection 2D seismic reflection data. The largest difference in the reflection coefficient ( $\Delta RC$ ) is spatially correlated with the seabed reflectivity anomalies determined for Day 12 and Day 13. (e) The reflection coefficient map at Day 34. The seabed reflectivity shows an increase within the seismic chimney (pink polygon), extending outside of the chimney, to further north within the study area. Mean values of reflection coefficients within and outside the area affected by chimneys are shown in Table 4.

in the reflection coefficient within the area of seismic chimneys. To the north-west of the area, the change in the reflection coefficient appears to be consistent between Day 12 and Day 13 (Fig. 11a and b). The variations in the Horizon 2 reflectivity between Day 12 and Day 13 occur mostly to the east and south of the diffuser (Fig. 11a and b). It is worth noting that Figs. 9–11 focus on the area affected by seismic chimneys at depth. Changes in the reflectivity within the entire survey area covered by all seismic lines are given in the Supplementary material, but are minor in comparison to those in the vicinity of the seismic chimneys.

The significant decrease in the reflection coefficient of Horizon 2 within the chimney area at Day 12 and Day 13 (Table 4), is interpreted to result from CO<sub>2</sub> injection deeper within the sediments, where upward migrating free gas is likely to cause a significant acoustic impedance contrast between gassy and gas-free sediments (Fig. 9c and d). The reduction in the reflection coefficient of Hori-

zon 2, both within and outside the seismic chimney area at Day 34, is interpreted to be caused by free gas within the overburden, and the spatial extent of the area with decreased reflection coefficient (Fig. 9e) is consistent with the area of enhanced acoustic impedance contrast mapped from the boomer dataset (Fig. 6b). Further, the CO<sub>2</sub> distribution within the chimney area is uneven at Day 12 and Day 13, emphasising the temporal variation of preferential gas migration pathways within the subsurface at this time (Fig. 9c–d and Fig. 11a–d). The experimental simulation of the migration of free gas within porous sediments (Chadwick, pers. comm.) has shown that free gas migrates upwards through alternating pathways within the overburden, confirming the patchy distribution of a network of acoustic anomalies within the overall chimney area, detected in this study (Fig. 9c–d and Fig. 11a–d).

The increase in the seabed reflectivity from Day 12 onwards is most likely caused by free gas within the pore space of

**Table 4**  
Mean reflection coefficient for the seabed and Horizon 2 observed on different days relative to the area affected by seismic chimneys on Day 12 for Day 12 and Day 13, and on Day 34 for Day 34. Note that there is no significant variation in the mean reflection coefficient prior to gas release (Day minus 2) across the area. Gas release increases the reflectivity of the seabed, but also causes a polarity reversal on Horizon 2 within the area affected by chimneys at depth. The larger standard deviations for Horizon 2 reflectivities at Day 12 and Day 13 inside the chimney area are possibly related to the uneven gas distribution within the chimney.

Day	Seabed mean reflection coefficient		Horizon 2 mean reflection coefficient	
	Inside chimney	Outside chimney	Inside chimney	Outside chimney
Day minus 2	0.21 (+/–0.03)	0.21 (+/–0.03)	0.04 (+/–0.01)	0.04 (+/–0.01)
Day 12	0.38 (+/–0.09)	0.37 (+/–0.07)	–0.12 (+/–0.10)	0.11 (+/–0.05)
Day 13	0.39 (+/–0.12)	0.27 (+/–0.14)	–0.10 (+/–0.08)	0.11 (+/–0.05)
Day 34	0.18 (+/–0.03)	0.15 (+/–0.03)	–0.11 (+/–0.04)	0.05 (+/–0.03)

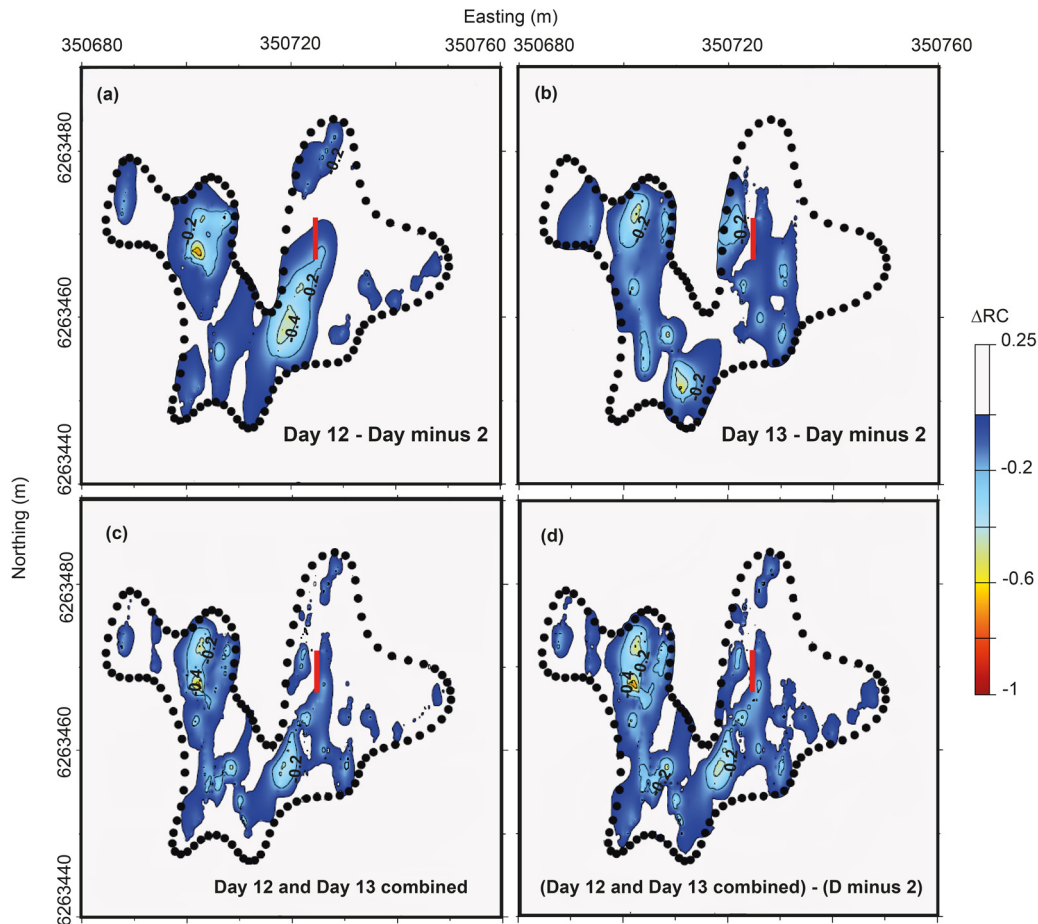


**Fig. 11.** Changes in Horizon 2 reflection coefficients ( $\Delta RC$ ) between Chirp surveys. (a) The difference in the reflection coefficient ( $\Delta RC$ ) between pre-release and Day 12 2D seismic reflection data, showing a significant reduction in the reflectivity of Horizon 2 within the chimney area (black polygon). (b) The difference in the reflection coefficient ( $\Delta RC$ ) between pre-release 2D seismic data and Day 13 2D seismic reflection data, revealing the decrease in reflection coefficient of Horizon 2 within the seismic chimney. (c) Combined reflection coefficient values for Horizon 2 within the chimney area, using reflectivity values calculated from Day 12 and Day 13. (d) The difference in the reflection coefficient ( $\Delta RC$ ) between the combined reflection coefficient anomaly and the pre-release 2D seismic reflection dataset, illustrating the overall difference in Horizon 2 reflectivity due to  $CO_2$  injection. The diffuser is indicated by the red line.

sediments just beneath the seabed (Fig. 10b–e). It is interesting to note that these seabed changes occur further north than the changes at depth, which might be related to the presence of shallow lateral conduits moving the gas up-dip (Fig. 10b–e). Previous studies have shown that change in the acoustic impedance is controlled by the distribution of free gas within the overburden, where thin gas-charged layers might lead to normal polarity, as the individual reflections of gas are indistinguishable, where the thickness of the gassy layer is less than one-eighth of the predominant wavelength (Widess, 1973; Geletti and Busetti, 2011; Ker et al., 2014). For this study, the thickness of the gassy layer should be equal or less than 1.25 cm to cause such effect, which is believed to be highly unlikely. Additionally, these seabed reflection coefficient anomalies are not randomly located within the overburden: they are spatially correlated with the Horizon 2 reflection coefficient anomalies (Fig. 9c–d and Fig. 10b–d), proving that despite the lack of clear acoustic evidence of free gas between Horizon 2 and the seabed, free gas migrated through sediments above Horizon 2 at this time. The spatial extent of the seabed reflectivity changes on Day 34 corresponds to the area with gas streams and pockmarks imaged on the multibeam bathymetry (Fig. 5 and Fig. 10e).

Synthetic seismograms produced using a temporally varying reflectivity model of the subsurface, and realistic source signatures, can be used together to validate our interpretation of changing acoustic properties during gas propagation. Reflectivities derived for the seabed and Horizon 2 (Table 4) on different days were con-

involved with chirp or boomer source signatures to produce synthetic seismograms that could be compared with real data. This comparison was done for the same small area outside (Fig. 12a) and inside the chimney (Fig. 12b) areas, which was sampled on all 2D seismic reflection surveys. Care was taken so that the synthetic and real data were processed using identical simple processing schemes. There is a good agreement between the synthetic and real data for each survey day (Fig. 12a and b), including the development of negative polarity reflections on Horizon 2 (Fig. 12b, Days 12–34), confirming the robustness of changes in reflection coefficient given in Table 4.

#### 4.3.2. Attenuation

The spectral-ratio technique described in Section 3.2 was applied to the 2D seismic reflection data to determine temporal and spatial variations in the  $Q$  values (Fig. 13; Table 5). The analysis focussed largely on the near-surface sediments between the seabed and Horizon 2, where the technique could be straightforwardly applied. It was more difficult to derive  $Q$  values for sediments below Horizon 2 due to the interference of the seabed multiple. To increase robustness of the results,  $Q_{\text{mean}}$  for a specific sediment package was calculated, averaging individual  $Q$  estimates from adjacent 2D seismic lines acquired on the same day.

Analysis of the chirp data prior to release (Day minus 2) shows distinct values of  $Q$  above and below Horizon 2 throughout the survey area, ranging between 83–114 above Horizon 2 ( $Q_{\text{mean}} = 98$ ), and 190–212 below Horizon 2 ( $Q_{\text{mean}} = 198$ ; Fig. 13a and d; Table 5).

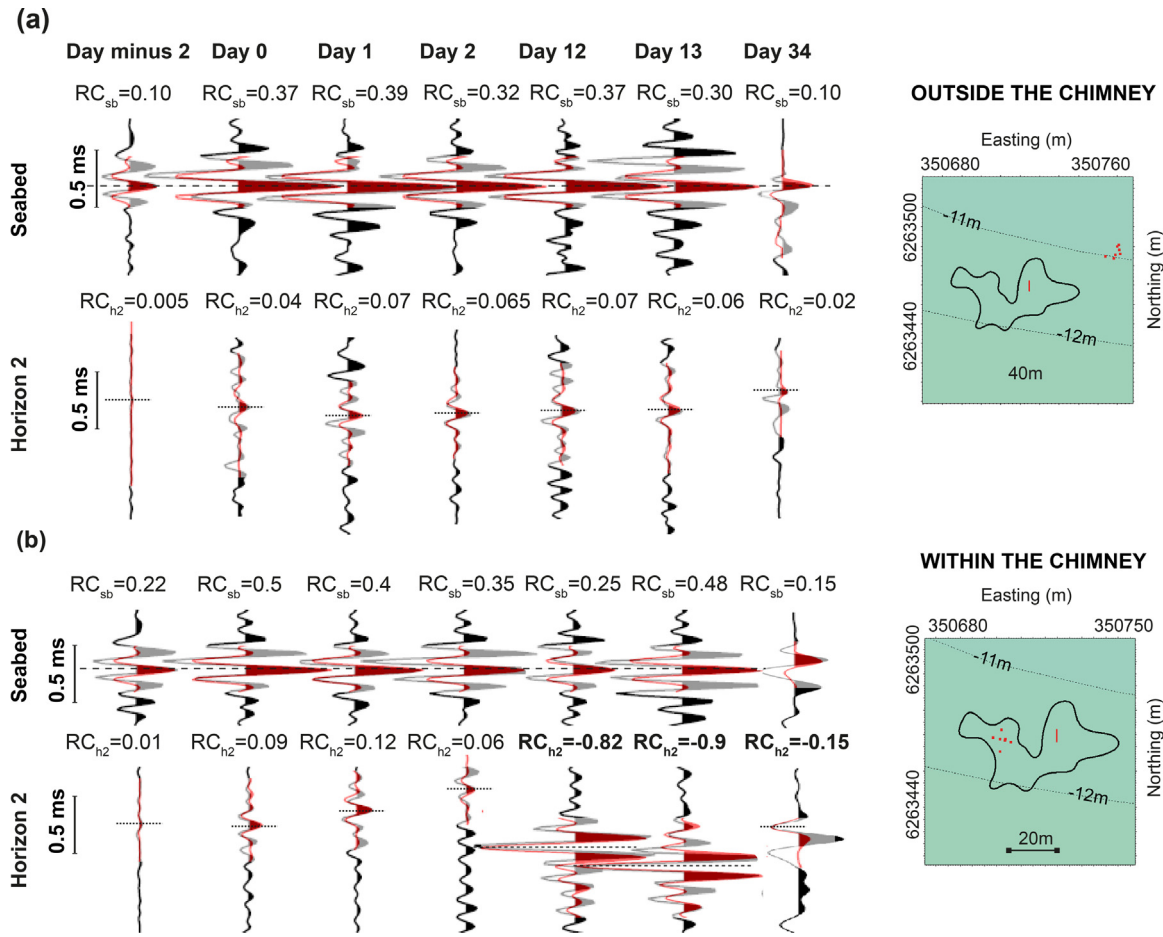


**Fig. 12.** Comparison of synthetic and real seismograms for different days during the release experiment. (a) Outside of area affected by seismic chimneys on Day 12. (b) Inside of area affected by seismic chimneys on Day 12. Note the good agreement between the real and synthetic data including where Horizon 2 becomes negative polarity due to the presence of gas within the chimney area. See main text for explanation of generation of synthetic seismograms. Real data and synthetic data are shown by the black and red wiggle traces, respectively. Location of the real wiggle traces (red dots) and the reflection coefficient values for the seabed ( $RC_{sb}$ ) and Horizon 2 ( $RC_{h2}$ ) used to produce synthetic seismograms are also shown. All wiggle traces are normalised.

At Day 12 when the  $Q$  analysis was repeated in the zone of seismic chimneys,  $Q$  was significantly reduced (43%) for sediments above Horizon 2 compared to the pre-release values ( $Q$  range 55.2–56.1;  $Q_{mean} = 55.6$ ; Fig. 13b, Table 5). A very similar reduction (42%) in  $Q$  for sediments above Horizon 2 in the chimney zone was also observed for Day 34 ( $Q_{mean} = 56.6$ ; Fig. 13c, Table 5). On Day 34,  $Q$  for sediments between Horizon 2 and the base of the layered sedimentary infill was 21% lower than the pre-release values, although this estimate is affected by large error bars ( $Q_{mean} = 157$ ; Fig. 13e; Table 5).

The amplitude spectrum of high frequency 2D seismic reflection data can be affected by the presence of gas, as gas bubbles can resonate at certain frequencies, scattering the incident sound energy. This was demonstrated by comparing the amplitude spectrum of chirp data acquired on different days for the seabed-Horizon 2

interval, both in areas affected by seismic chimneys and those that are not (Fig. 14). The spectral content of the 2D seismic data outside the chimney area is quite similar throughout the survey, with the dominant frequency at  $-30$  dB being 7270 ( $\pm 65$ ) Hz between Day 0 and Day 13 (Fig. 14a and c). However, for 2D seismic data within the seismic chimney zone, the dominant frequency at  $-30$  dB is 7260 ( $\pm 60$ ) Hz at Day 0 and Day 1, reducing to 7190 ( $\pm 30$ ) Hz at Day 2, 7065 ( $\pm 80$ ) Hz at Day 12, and 6695 ( $\pm 80$ ) Hz at Day 13 (Fig. 14b and c). This suggests that the higher frequency components of the seismic data are more attenuated than the low frequency components from Day 2 onwards within the seismic chimney area, leading to a dominant frequency shift towards lower frequencies (Fig. 14c).

A close relationship between  $Q$  and mean-grain size ( $\Phi$ ) of sediments has been previously reported (Shumway, 1960; Hamilton, 1972; Guigné et al., 1989; Pinson et al., 2008).  $Q$  values less than

**Table 5**  
Variation of the Quality factor ( $Q_{mean}$ ) above and below Horizon 2 observed on different survey days, within and outside the chimney area. The change in  $Q_{mean}$  on Day minus 2, within and outside the chimney area, above and below Horizon 2, is consistent with the change in grain size from sandy to muddy sediments. Injection of gas decreases  $Q_{mean}$  throughout the sediment column above the diffuser, within the chimney area. Note that  $Q_{mean}$  measurements above Horizon 2 outside the chimney area are similar to pre-release values. Note also that  $Q_{mean}$  values below Horizon 2 within the chimney are associated with larger errors.

Day	$Q_{mean}$ (inside the chimney)		$Q_{mean}$ (outside the chimney)
	Above Horizon 2	Below Horizon 2	Above Horizon 2
Day minus 2	98 (+15/–10)	198 (+13/–11)	103 (+12/–9.4)
Day 12	56.1 (+17/–10)	No robust values	108 (+25/–10)
Day 34	56.6 (+17/–10)	157 (+27/–19)	No robust values

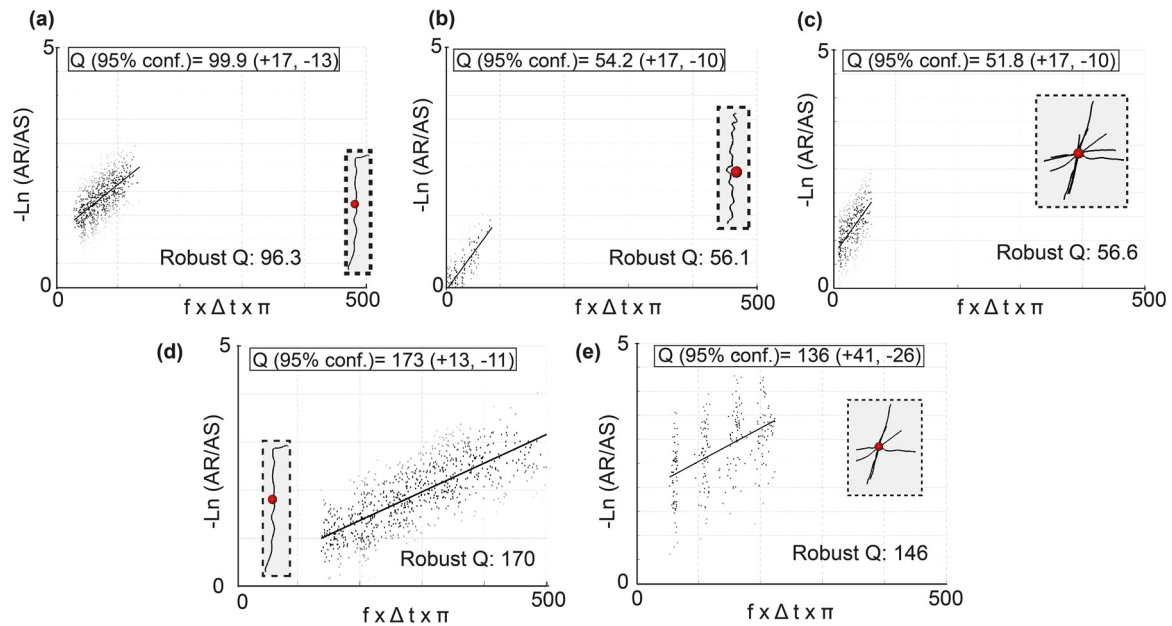


**Fig. 13.** The temporal variation of  $Q$  during the QICS experiment. (a)  $Q$  above Horizon 2 prior to  $\text{CO}_2$  release.  $Q$  is 96.3 above Horizon 2. (b)  $Q$  above Horizon 2 at Day 12. There is a significant decrease in  $Q$  above Horizon 2, in the order of 43% (from  $Q_{\text{mean}} = 98$  at Day minus 2 to  $Q = 56.1$  at Day 12). (c)  $Q$  above Horizon 2 at Day 34.  $Q$  above Horizon 2 has decreased by 42% (from  $Q_{\text{mean}} = 98$  at Day minus 2 to  $Q = 56.6$  at Day 34). (d)  $Q$  between the seabed and the base of the layered sequence at Day minus 2. Knowing the depth between surfaces,  $Q$  between Horizon 2 and the base of the layered sequence was inferred as 192 at Day minus 2. (e)  $Q$  between seabed and the base of the layered sequence was inferred as 157, suggesting a decrease by 21% below Horizon 2 at Day 34. Note the larger error bars for this calculation. 2D seismic lines used in  $Q$  analysis are given inset, indicated by black lines, as well as the diffuser (the dark gray dot).

75 are attributed to granular, sandy and coarse silty sediments ( $\Phi < 6$ ), while  $Q$  values larger than 75 are associated with finer silts and clay-dominated sediments ( $\Phi > 6$ ) that deform as a coherent matrix rather than a granular medium.  $Q$  analysis from pre-release 2D seismic data is consistent with previous core grain-size analysis in Ardmucknish Bay (Fig. 2), where sediments above Horizon 2 (Fig. 13a) are coarser-grained silty-sands ( $Q_{\text{mean}} = 98$ ; Table 5), and sediments underlying Horizon 2 (Fig. 13d) are finer-grained muddy sediments with a high clay content ( $Q_{\text{mean}} = 198$ ; Table 5). Although a  $Q_{\text{mean}} = 98$  is indicative of some finer fraction content above Horizon 2, the contrast with a  $Q_{\text{mean}} = 198$  below Horizon 2 is indicative of a significant contrast in grain size distribution between these two facies.

The seismic quality factor (or attenuation) has been shown to be useful in determining the presence of free gas within sediments, as well as providing more quantitative estimates including gas saturation (Hamilton, 1972; White, 1975; Mavko and Nur, 1979; Winkler and Nur, 1979; Carcione and Picotti, 2006; Rossi et al., 2007; Morgan et al., 2012). Seismic quality factors are observed to decrease (i.e. increased levels of attenuation) in response to relatively low level of free gas (<20%) within the pore space (Morgan et al., 2012). The presence of gas within the pore space dramatically alters the mesoscopic fluid flow (Johnson et al., 2002; Quintal et al., 2011), which has a major influence on the attenuation of seismic waves (Müller et al., 2010). The decrease of the seismic quality factor above Horizon 2, on the order of 42–43% (Table 5; Fig. 13b and c) is interpreted as being the result of free gas within the upper acoustically transparent unit, for the period Days 12–34. Similarly, the decrease in  $Q$  below Horizon 2 at Day 34 is probably caused by upward migrating  $\text{CO}_2$  within the seismic chimneys (Table 5; Fig. 13e). The consistency of observed  $Q$  values for the period Days 12–34 (Table 5; Fig. 13b and c) probably indicates that the gas saturation above Horizon 2 remained approximately constant.

The low-frequency-shift of the recorded spectrum has also been observed in other studies, where the low velocity gas charged sediments have been interpreted to cause increased attenuation of high-frequencies (Quan and Harris, 1997; Tréhu and Flueh, 2001;

Rossi et al., 2007). The frequency-dependant decrease in seismic amplitudes detected from Day 2 onwards within the seismic chimney zone is thus interpreted to be due to  $\text{CO}_2$  fluxing through the sediments, and causing changes in the sediment acoustic properties (Fig. 14a–c).

## 5. Discussion

Our experiment has shown that 2D seismic reflection surveying can indicate probable gas migration pathways in shallow marine sediments, and associated changes in acoustic properties. The temporal variation in sediment acoustic properties, and correlation with the cumulative injected  $\text{CO}_2$  are summarised in Fig. 15. Here, we discuss possible mechanisms controlling  $\text{CO}_2$  migration, before emphasizing the importance of reflection coefficient and attenuation analysis from 2D seismic reflection data for improving free gas detection within near-surface sediments.

### 5.1. Mechanisms controlling $\text{CO}_2$ migration

Bubble growth within under-consolidated soft sediments emphasizes grain-size control on gas invasion. Mechanical response of sediments to rising bubbles differs significantly, with coarse-grained sandy sediments favouring capillary invasion and fluidisation, while fracturing dominates in fine-grained media (Boudreau et al., 2005; Best et al., 2006; Jain and Juanes, 2009). In coarse-grained sandy sediments, rising bubbles percolate into the inter-granular pore space leading to sediment fluidisation, whereas in fine-grained muddy sediments, grains are forced apart by migrating bubbles, leading to the initiation and propagation of a fracture. Although perceived pliability of muddy sediments counteracts their elastic behaviour in response to rising bubbles, the eccentric oblate spheroid shape of bubbles microscopically imaged within muddy sediments (Barry et al., 2010), can only be explained if the mechanical response of these sediments follows Linear elastic fracture mechanics theory (LEFM) (Anderson et al., 1998; Johnson et al., 2002; Best et al., 2004; Barry et al., 2010; Katsman et al.,

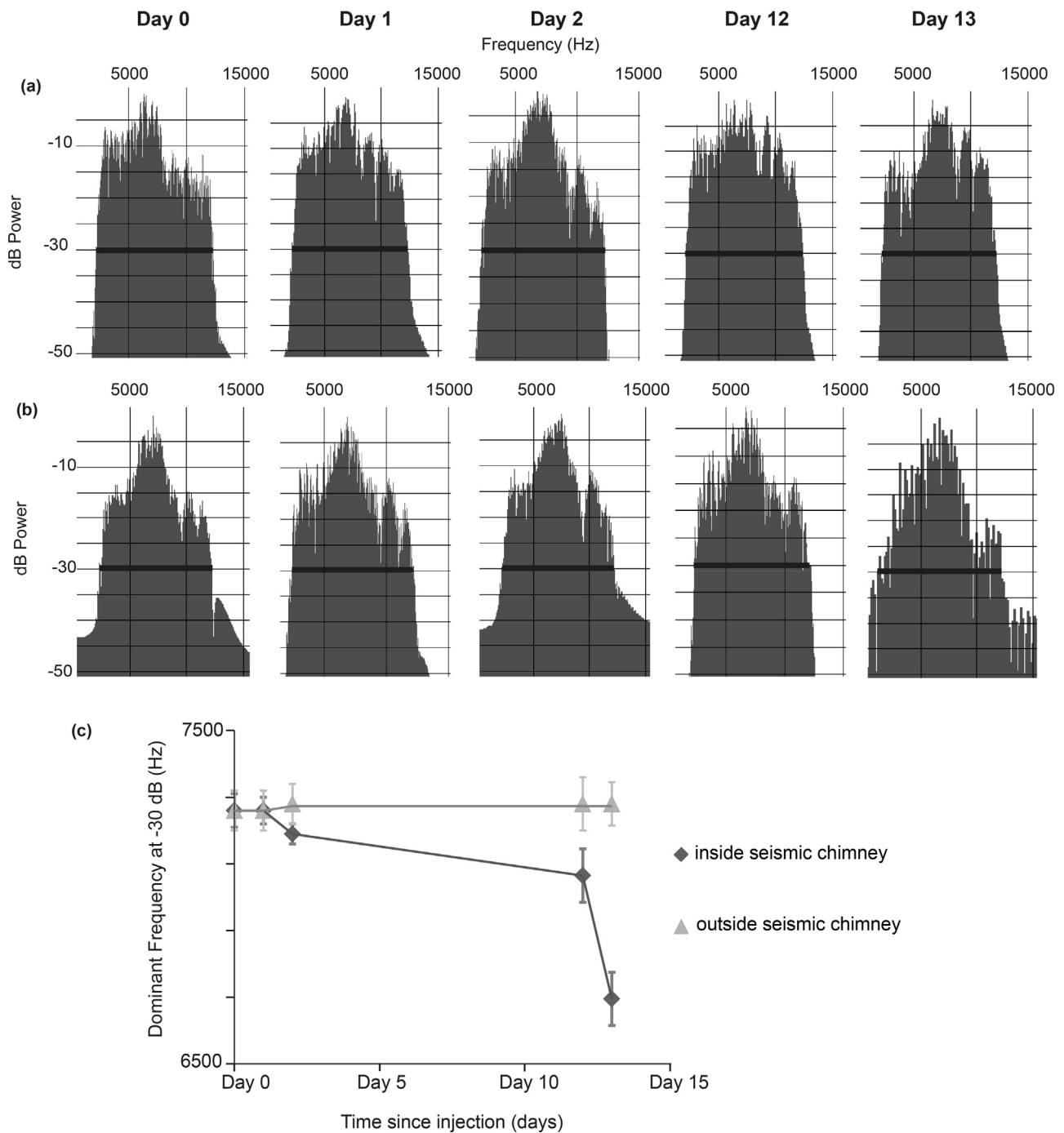


**Fig. 14.** Temporal and spatial variation of the seismic amplitude spectrum of Chirp data. (a) Amplitude spectrum of the seismic data outside the chimney area (developed on Day 12) for the seismic traces shown at Fig. 12a. The dominant frequency at  $-30$  dB is  $7270$  ( $\pm 65$ ) Hz for Days 0–13. (b) Amplitude spectrum of the 2D seismic data within the chimney area for the seismic traces shown at Fig. 12b. The dominant frequency at  $-30$  dB is  $7260$  ( $\pm 60$ ) Hz at Day 0 and Day 1, and reduces to  $7190$  ( $\pm 30$ ) Hz at Day 2,  $7065$  ( $\pm 80$ ) Hz at Day 12, and  $6695$  ( $\pm 80$ ) Hz at Day 13, revealing the increased attenuation of high frequencies in the presence of free gas. (c) The temporal variation of the dominant frequency of the 2D seismic data (at  $-30$  dB) outside and inside of the area affected by chimneys.

2013). Additionally, buoyancy-driven hydro-fracturing occurs as a response to the relative motion of fluids against solids, including magma intrusion, migration of hydrocarbons, and metamorphic water through porous media (Lister, 1990; Dahm, 2000; Menand and Tait, 2002; Nunn and Meulbroek, 2002; Levine et al., 2009; Fall et al., 2012). During laboratory experiments, recorded bubble internal pressure suggests a cyclicity, with increasing pressures related to gas injection, and pressure decrease due to sediment fracturing (Johnson et al., 2002).

Based on previous research on gas migration mechanisms within under-consolidated sediments, as well as analysis of temporal and spatial evolution of the acoustic anomalies from our 2D seismic dataset, we interpret that  $\text{CO}_2$  migration is predominantly controlled by the grain-size of the surrounding sediments in the initial period of the release, whereas in the later stages, the  $\text{CO}_2$  injection rate or total volume injected probably become the dominant factors (Fig. 8). In the early phases, up to Day 13, seismic chimneys detected below Horizon 2 are interpreted as

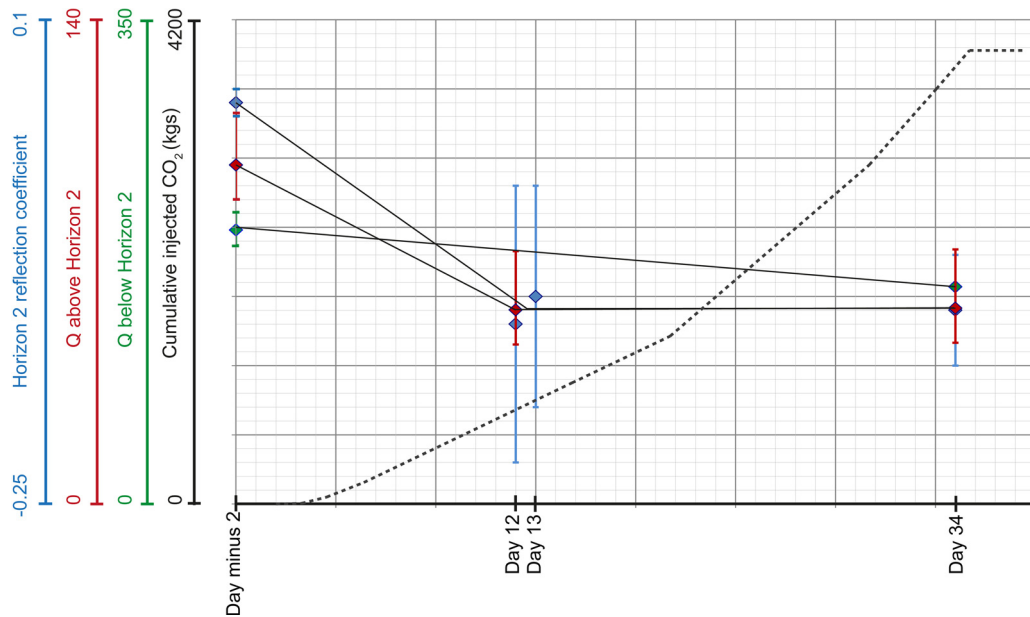


**Fig. 15.** Changes in the reflection coefficient of Horizon 2, quality factor ( $Q$ ) above and below Horizon 2, and cumulative amount of  $\text{CO}_2$  injected during the experiment. Sampling points are indicated as circles (Horizon 2 reflection coefficient), stars ( $Q$  above Horizon 2), and squares ( $Q$  below Horizon 2). Due to increasing  $\text{CO}_2$  within the overburden, the reflection coefficient for Horizon 2 decreases, while attenuation increases above and below Horizon 2. The cumulative amount of injected  $\text{CO}_2$  is indicated by bold dashed line.

inter-connected micro-scale fractures within the muddy sediments (Fig. 8b and c). The change in the grain-size from silty-clayey sediments below Horizon 2 to sandy-silty sediments above it possibly caused a change in the  $\text{CO}_2$  migration pattern, from fracture-dominated regime to capillary invasion and fluidisation. Seismic chimneys reaching the seabed on Day 34 (Table 1) are interpreted to demonstrate that either  $\text{CO}_2$  injection rate or the total volume injected become the dominant factors controlling  $\text{CO}_2$  migration later in the experiment (Fig. 8d).  $\text{CO}_2$  transport occurs by vertical channelling from the diffuser up to seabed in spite of grain-size differences within the travelled media. As there is no seismic data collected between Day 13 and Day 34, it is not possible to determine the critical injection rate/total volume needed to move from stratigraphic control on  $\text{CO}_2$  migration. However, the injection rate at Day 34 ( $210 \text{ kgs day}^{-1}$ ) or the total volume injected by Day 34 (3600 kgs) is proposed as possible upper limits (Table 1).

## 5.2. Improvements in $\text{CO}_2$ detection within the subsurface

It is crucial to note that, unlike fracture identification, capillary invasion of  $\text{CO}_2$  above Horizon 2 is not seismically resolvable as a distinct and continuous change in the seismic reflection amplitudes, despite the high resolution (i.e. centimetre scale) of our seismic reflection dataset (Fig. 8a–d). This observation is fundamental for CCS operations where time-lapse 3D seismic reflection data, with significantly lower vertical resolution compared to the 2D seismic dataset used in this study, is commonly used to track and assure safe storage of  $\text{CO}_2$  within the reservoir. In the case of Sleipner CCS site, where  $\text{CO}_2$  has been injected into the Utsira Formation since 1996, at a rate of  $1 \text{ Mt/year}$ , time-lapse seismic surveys demonstrate that the injected  $\text{CO}_2$  is securely confined within the Utsira Formation, as there is no contrast of acoustic impedance imaged above the topmost layer of the Utsira Sand (Arts et al., 2008; Chadwick et al., 2010). Our study clearly demonstrates that free gas can be present within the overburden without presenting a classical seismic reflection indicator, i.e. continuous high-amplitude, polarity-reversed reflection. However, the analysis of reflection coefficient for the seabed and increased seismic

attenuation between the seabed and Horizon 2 are supportive of the presence of free gas above Horizon 2.

Risk assessment and storage verification rely on high-resolution seismic imaging of the shallow overburden, as well as traditional, lower-frequency imaging at reservoir depths. Our results indicate that the traditional qualitative interpretive approach based on the mapping of high-amplitude, polarity-reversed reflections may not be sufficient to reliably track the upward migration of free gas in the event of leakage, and the interpretations can be significantly improved and validated by the analysis of reflection coefficient and seismic attenuation calculations.

## 6. Conclusion

In this first controlled  $\text{CO}_2$  release experiment, where  $\text{CO}_2$  was injected into under-consolidated, shallow marine sediments over 37 days, repeated 2D seismic reflection surveys imaged the propagation of gas through the subsurface and into the water column. Analysis of the 2D seismic reflection data, acquired pre-release and syn-release, led to the following conclusions:

- Local stratigraphy influenced  $\text{CO}_2$  migration in subsurface sediments around the diffuser, and comprised c. 1.5 m thick layer of coarse-sand and gravel, above a c. 2 m thick fine-sand layer. These two acoustically transparent units overlie a c. 15 m layered muddy sequence with sub-parallel reflections (Fig. 4; Table 2). The boundary between this mud sequence and the overlying fine-sand forms a characteristic erosional unconformity (Horizon 2).
- This erosional unconformity, Horizon 2, was found to partially trap the injected  $\text{CO}_2$  in the early stages of the experiment, revealed by enhanced reflectivity and seismic chimneys imaged beneath the unconformity (Fig. 8a–c). Following an increase in the amount of injected  $\text{CO}_2$  later on in the experiment (Table 1), seismic chimneys previously confined within the layered sequence reached the seabed, leading to  $\text{CO}_2$  leakage into the water column (Fig. 8d). We argue that in the early stages of the experiment, up to Day 13, capillary invasion and fluidisation were the main mechanisms allowing  $\text{CO}_2$  migration above Horizon 2 within sandy

sediments, while fracture initiation and propagation facilitated gas migration in the lower fine-grained sediment. Unconformity Horizon 2 trapped the majority of the gas until either increases in gas pressure or increases in the total volume of CO<sub>2</sub> led to seismic chimneys reaching the seabed, overriding stratigraphic control.

- Following CO<sub>2</sub> injection, changes in the reflection coefficient of the seabed and Horizon 2, as well as seismic attenuation within the near-surface sediments were identified (Tables 4 and 5). The reflection coefficient of Horizon 2 decreased and became negative polarity within the seismic chimney area (Fig. 15; Table 4). The seismic quality factor, *Q*, decreased during the release by 42–43% above Horizon 2, and 21% below Horizon 2 within the chimney area. The variations in the reflection coefficient and *Q* identified from 2D seismic reflection data demonstrate that we can efficiently track CO<sub>2</sub> propagation by its impact on sediment acoustic properties.
- The assessment of the changes in the reflection coefficient and seismic attenuation from the seismic reflection data is complementary to traditional seismic interpretation, enhancing and validating CO<sub>2</sub> detection within the subsurface, and allowing a better understanding of the impact of CO<sub>2</sub> on sediment acoustic properties. On-going work is focused on improving estimates of gas content within the sediment pore space by the inversion of the reflection coefficient and attenuation values, together with an appropriate rock physics model which describes accurately the physical properties of surrounding sediments, and gas distribution within the pore space.

## Acknowledgments

We acknowledge funding from NERC (NE/H013962/1), the Scottish government and the European Union. We thank the crew of research vessels *Seol Mara* and *White Ribbon*, John Davis for technical assistance with geophysical data acquisition, Alice Tan for sediment analysis, and Craig Wallace of Kongsberg Ltd. for provision and processing of the multibeam data. The *White Ribbon* surveys were funded by the BGS Maremap project.

## Appendix A. Supplementary data

Supplementary data associated with this article can be found, in the online version, at <http://dx.doi.org/10.1016/j.ijggc.2015.03.005>.

## References

- Anderson, A., Abegg, F., Hawkins, J., Duncan, M., Lyons, A., 1998. Bubble populations and acoustic interaction with the gassy floor of Eckernförde Bay. *Cont. Shelf Res.* 18, 1807–1838.
- Anstey, N., 1977. *Seismic Interpretation: The Physical Aspects: Being a Record of the Short Course, The New Seismic Interpreter*. International Human Resources Development Corporation.
- Arts, R., Chadwick, A., Eiken, O., Thibeau, S., Nooner, S., 2008. Ten years' experience of monitoring CO<sub>2</sub> injection in the Utsira Sand at Sleipner, offshore Norway. *First Break* 26.
- Bachu, S., 2008. CO<sub>2</sub> storage in geological media: role, means, status and barriers to deployment. *Prog. Energy Combust. Sci.* 34, 254–273.
- Baristean, N., Anka, Z., Di Primio, R., Rodriguez, J., Marchal, D., Dominguez, F., 2012. Distribution of hydrocarbon leakage indicators in the Malvinas Basin, offshore Argentine continental margin. *Mar. Geol.* 332, 56–74.
- Barry, M., Boudreau, B., Johnson, B., Reed, A., 2010. First-order description of the mechanical fracture behavior of fine-grained surficial marine sediments during gas bubble growth. *J. Geophys. Res.: Earth Surf.* 115, F04029.
- Benson, S.M., Hepple, R., Apps, J., Tsang, C.-F., Lippmann, M., 2002. Lessons Learned from Natural and Industrial Analogues for Storage of Carbon Dioxide in Deep Geological Formations. Earth Sciences Division, E.O. Lawrence Berkeley National Laboratory, Berkeley, pp. 135.
- Berges, B.J., Leighton, T.G., White, P.R., 2015. Passive acoustic quantification of gas fluxes during controlled gas release experiments. *Int. J. Greenhouse Gas Control*, <http://dx.doi.org/10.1016/j.ijggc.2015.02.008>.
- Best, A.I., Tuffin, M.D., Dix, J.K., Bull, J.M., 2004. Tidal height and frequency dependence of acoustic velocity and attenuation in shallow gassy marine sediments. *J. Geophys. Res.: Solid Earth* 109, B08101.
- Best, A.I., Richardson, M.D., Boudreau, B.P., Judd, A.G., Leifer, I., Lyons, A.P., Martens, C.S., Orange, D.L., Wheeler, S.J., 2006. Shallow seabed methane gas could pose coastal hazard. *Eos Trans. Am. Geophys. Union* 87, 213–217.
- Blackford, J., Stahl, H., Bull, J.M., Berges, B.J.P., Cevatoglu, M., Lichtschlag, A., Connelly, D., James, R.H., Kita, J., Long, D., Naylor, M., Shitashima, K., Smith, D., Taylor, P., Wright, I., Akhurst, M., Chen, B., Gernon, T.M., Hauton, C., Hayashi, M., Kaieda, H., Leighton, T.G., Sato, T., Sayer, M.D.J., Suzumura, M., Tait, K., Vardy, M.E., White, P.R., Widdicombe, S., 2014. Detection and impacts of leakage from sub-seafloor deep geological carbon dioxide storage. *Nat. Clim. Change* 4, 1011–1016, <http://dx.doi.org/10.1038/nclimate2381>.
- Boudreau, B.P., Algar, C., Johnson, B.D., Croudace, I., Reed, A., Furukawa, Y., Dorgan, K.M., Jumars, P.A., Grader, A.S., Gardiner, B.S., 2005. Bubble growth and rise in soft sediments. *Geology* 33, 517–520.
- Bull, J.M., Quinn, R., Dix, J.K., 1998. Reflection coefficient calculation from marine high resolution seismic reflection (Chirp) data and application to an archaeological case study. *Mar. Geophys. Res.* 20, 1–11.
- Carcione, J.M., Picotti, S., 2006. P-wave seismic attenuation by slow-wave diffusion: effects of inhomogeneous rock properties. *Geophysics* 71, O1–O8.
- Cathles, L., Su, Z., Chen, D., 2010. The physics of gas chimney and pockmark formation, with implications for assessment of seafloor hazards and gas sequestration. *Mar. Petrol. Geol.* 27, 82–91.
- Celia, M.A., Nordbotten, J.M., 2009. Practical modeling approaches for geological storage of carbon dioxide. *Ground Water* 47, 627–638.
- Chadwick, A., Williams, G., Delepine, N., Clochar, V., Labat, K., Sturton, S., Buddensiek, M.-L., Dillen, M., Nickel, M., Lima, A.L., 2010. Quantitative analysis of time-lapse seismic monitoring data at the Sleipner CO<sub>2</sub> storage operation. *The Leading Edge* 29, 170–177.
- Dahm, T., 2000. On the shape and velocity of fluid-filled fractures in the Earth. *Geophys. J. Int.* 142, 181–192.
- Damen, K., Faaij, A., Turkenburg, W., 2006. Health, safety and environmental risks of underground CO<sub>2</sub> storage – overview of mechanisms and current knowledge. *Clim. Change* 74, 289–318.
- Fall, A., Eichhubl, P., Cumella, S.P., Bodnar, R.J., Laubach, S.E., Becker, S.P., 2012. Testing the basin-centered gas accumulation model using fluid inclusion observations: Southern Piceance Basin, Colorado. *AAPG Bull.* 96, 2297–2318.
- Geletti, R., Busetti, M., 2011. A double bottom simulating reflector in the western Ross Sea Antarctica. *J. Geophys. Res.: Solid Earth* 116, B04101.
- Guigné, J.Y., Pace, N.G., Chin, V.H., 1989. Dynamic extraction of sediment attenuation from subbottom acoustic data. *J. Geophys. Res.: Solid Earth* 94, 5745–5755.
- Gutowski, M., Bull, J., Henstock, T., Dix, J., Hogarth, P., Leighton, T., White, P., 2002. Chirp sub-bottom profiler source signature design and field testing. *Mar. Geophys. Res.* 23, 481–492.
- Hamilton, E.L., 1972. Compressional-wave attenuation in marine sediments. *Geophysics* 37, 620–646.
- Howe, J.A., Shimmield, T., Austin, W.E., Longva, O., 2002. Post-glacial depositional environments in a mid-high latitude glacially-overdeepened sea loch, inner Loch Etive, western Scotland. *Mar. Geol.* 185, 417–433.
- Jain, A., Juanes, R., 2009. Preferential mode of gas invasion in sediments: Grain-scale mechanistic model of coupled multiphase fluid flow and sediment mechanics. *J. Geophys. Res.: Solid Earth* 114, B08101.
- Johnson, B.D., Boudreau, B.P., Gardiner, B.S., Maass, R., 2002. Mechanical response of sediments to bubble growth. *Mar. Geol.* 187, 347–363.
- Katsman, R., Ostrovsky, I., Makovsky, Y., 2013. Methane bubble growth in fine-grained muddy aquatic sediment: insight from modeling. *Earth Planet. Sci. Lett.* 377, 336–346.
- Katzer, J., Moniz, E., Deutch, J., Ansolabehere, S., Beer, J., 2007. The future of coal: an interdisciplinary MIT study. In: Technical Report. Massachusetts Institute of Technology, Cambridge, MA.
- Ker, S., Le Gonidec, Y., Marsset, B., Westbrook, G.K., Gibert, D., Minshull, T.A., 2014. Fine-scale gas distribution in marine sediments assessed from deep-towed seismic data. *Geophys. J. Int.*, ggt497.
- Lackner, K.S., Brennan, S., 2009. Envisioning carbon capture and storage: expanded possibilities due to air capture, leakage insurance, and C-14 monitoring. *Clim. Change* 96, 357–378.
- Levine, J.S., Matter, J.M., Goldberg, D., Lackner, K.S., 2009. Gravitational trapping of carbon dioxide in deep ocean sediments: hydraulic fracturing and mechanical stability. *Energy Procedia* 1, 3647–3654.
- Lister, J.R., 1990. Buoyancy-driven fluid fracture: the effects of material toughness and of low-viscosity precursors. *J. Fluid Mech.* 210, 263–280.
- Løseth, H., Gading, M., Wensaas, L., 2009. Hydrocarbon leakage interpreted on seismic data. *Mar. Petrol. Geol.* 26, 1304–1319.
- Mavko, G.M., Nur, A., 1979. Wave attenuation in partially saturated rocks. *Geophysics* 44, 161–178.
- McIntyre, K.L., Howe, J.A., 2010. Scottish west coast fjords since the last glaciation: a review. 344. Geological Society London Special Publications, pp. 305–329.
- Meldahl, P., Heggland, R., Bril, B., de Groot, P., 2001. Identifying faults and gas chimneys using multiattributes and neural networks. *The Leading Edge* 20, 474–482.
- Menand, T., Tait, S.R., 2002. The propagation of a buoyant liquid-filled fissure from a source under constant pressure: an experimental approach. *J. Geophys. Res.* 107, 2306.

- Metz, B., Davidson, O., de Coninck, H., Loos, M., Meyer, L., 2005. IPCC Special Report on Carbon Dioxide Capture and Storage. Intergovernmental Panel on Climate Change, Working Group III. Cambridge University Press, Cambridge, 442.
- Morgan, E.C., Vanneste, M., Lecomte, I., Baise, L.G., Longva, O., McAdoo, B., 2012. Estimation of free gas saturation from seismic reflection surveys by the genetic algorithm inversion of a P-wave attenuation model. *Geophysics* 77, R175–R187.
- Müller, T.M., Gurevich, B., Lebedev, M., 2010. Seismic wave attenuation and dispersion resulting from wave-induced flow in porous rocks – a review. *Geophysics* 75, 75A147–75A164.
- Nørgaard-Pedersen, N., Austin, W., Howe, J., Shimmield, T., 2006. The Holocene record of Loch Etive, western Scotland: influence of catchment and relative sea level changes. *Mar. Geol.* 228, 55–71.
- Nunn, J.A., Meulbroek, P., 2002. Kilometer-scale upward migration of hydrocarbons in geopressed sediments by buoyancy-driven propagation of methane-filled fractures. *AAPG Bull.* 86, 907–918.
- Petersen, C.J., Büinz, S., Hustoft, S., Mienert, J., Klaeschen, D., 2010. High-resolution P-Cable 3D seismic imaging of gas chimney structures in gas hydrated sediments of an Arctic sediment drift. *Mar. Petrol. Geol.* 27, 1981–1994.
- Pinson, L.J., Henstock, T.J., Dix, J.K., Bull, J.M., 2008. Estimating quality factor and mean grain size of sediments from high-resolution marine seismic data. *Geophysics* 73, G19–G28.
- Pires, J., Martins, F., Alvim-Ferraz, M., Simões, M., 2011. Recent developments on carbon capture and storage: an overview. *Chem. Eng. Res. Des.* 89, 1446–1460.
- Plaza-Faverola, A., Büinz, S., Mienert, J., 2011. Repeated fluid expulsion through sub-seabed chimneys offshore Norway in response to glacial cycles. *Earth Planet. Sci. Lett.* 305, 297–308.
- Quan, Y., Harris, J.M., 1997. Seismic attenuation tomography using the frequency shift method. *Geophysics* 62, 895–905.
- Quinn, R., Bull, J.M., Dix, J.K., 1998. Optimal processing of marine high-resolution seismic reflection (Chirp) data. *Mar. Geophys. Res.* 20, 13–20.
- Quintal, B., Steeb, H., Frehner, M., Schmalholz, S.M., 2011. Quasi-static finite element modeling of seismic attenuation and dispersion due to wave-induced fluid flow in poroelastic media. *J. Geophys. Res.: Solid Earth* 116, B01201.
- Rajan, A., Mienert, J., Büinz, S., 2012. Acoustic evidence for a gas migration and release system in Arctic glaciated continental margins offshore NW-Svalbard. *Mar. Petrol. Geol.* 32, 36–49.
- Rossi, G., Gei, D., Böhm, G., Madrussani, G., Carcione, J.M., 2007. Attenuation tomography: an application to gas-hydrate and free-gas detection. *Geophys. Prospect.* 55, 655–669.
- Schock, S.G., 2004. A method for estimating the physical and acoustic properties of the sea bed using chirp sonar data. *IEEE J. Oceanic Eng.* 29, 1200–1217.
- Shumway, G., 1960. Sound speed and absorption studies of marine sediments by a resonance method. *Geophysics* 25, 451–467.
- Spence, G., Minshull, T., Fink, C., 1995. Seismic studies of methane gas hydrate, offshore Vancouver Island. *Proceedings of the Ocean Drilling Program, Scientific Results* 146, 163–174.
- Sun, Q., Wu, S., Cartwright, J., Dong, D., 2012. Shallow gas and focused fluid flow systems in the Pearl River Mouth Basin, northern South China Sea. *Mar. Geol.* 315, 1–14.
- Taylor, P., Stahl, H., Vardy, M.E., Bull, J.M., Akhurst, M., Hauton, C., James, R.H., Lichtschlag, A., Long, D., Aleynik, D., 2015. A novel sub-seabed CO<sub>2</sub> release experiment informing monitoring and impact assessment for geological carbon storage. *Int. J. Greenhouse Gas Control*, <http://dx.doi.org/10.1016/j.ijggc.2014.09.007>.
- Tomasini, J., de Santa Ana, H., Johnson, A.H., 2010. Identification of new seismic evidence regarding gas hydrate occurrence and gas migration pathways offshore Uruguay. *Proceedings of the AAPG 2010 Annual Convention & Exhibition*.
- Tréhu, A.M., Flueh, E.R., 2001. Estimating the thickness of the free gas zone beneath Hydrate Ridge Oregon continental margin, from seismic velocities and attenuation. *J. Geophys. Res.: Solid Earth* 106, 2035–2045.
- Upham, P., Roberts, T., 2011. Public perceptions of CCS: emergent themes in pan-European focus groups and implications for communications. *Int. J. Greenhouse Gas Control* 5, 1359–1367.
- Warner, M., 1990. Absolute reflection coefficients from deep seismic reflections. *Tectonophysics* 173, 15–23.
- West, J.M., Pearce, J., Bentham, M., Maul, P., 2005. Issue profile: environmental issues and the geological storage of CO<sub>2</sub>. *Eur. Environ.* 15, 250–259.
- White, J., 1975. Computed seismic speeds and attenuation in rocks with partial gas saturation. *Geophysics* 40, 224–232.
- Widess, M., 1973. How thin is a thin bed? *Geophysics* 38, 1176–1180.
- Williams, K.L., Jackson, D.R., Thorsos, E.I., Tang, D., Schock, S.G., 2002. Comparison of sound speed and attenuation measured in a sandy sediment to predictions based on the Biot theory of porous media. *IEEE J. Oceanic Eng.* 27, 413–428.
- Winkler, K., Nur, A., 1979. Pore fluids and seismic attenuation in rocks. *Geophys. Res. Lett.* 6, 1–4.
- Yoo, D.G., Kang, N.K., Yi, B.Y., Kim, G.Y., Ryu, B.J., Lee, K., Lee, G.H., Riedel, M., 2013. Occurrence and seismic characteristics of gas hydrate in the Ulleung Basin, East Sea. *Mar. Petrol. Geol.* 47, 236–247.
- Zhang, Z., McConnell, D.R., Han, D.-H., 2012. Rock physics-based seismic trace analysis of unconsolidated sediments containing gas hydrate and free gas in Green Canyon 955, Northern Gulf of Mexico. *Mar. Petrol. Geol.* 34, 119–133.